RAPID MULTI-CONTRAST MAGNETIC RESONANCE IMAGING AND TIME-OF-FLIGHT ANGIOGRAPHY

A THESIS SUBMITTED TO
THE GRADUATE SCHOOL OF ENGINEERING AND SCIENCE
OF BILKENT UNIVERSITY
IN PARTIAL FULFILLMENT OF THE REQUIREMENTS FOR
THE DEGREE OF
MASTER OF SCIENCE
IN
ELECTRICAL AND ELECTRONICS ENGINEERING

By
Toygan Kılıç
January 2019

RAPID MULTI-CONTRAST MAGNETIC RESONANCE IMAGING AND TIME-OF-FLIGHT ANGIOGRAPHY

By Toygan Kılıç

January 2019

We certify that we have read this thesis and that in our opinion it is fully adequate, in scope and in quality, as a thesis for the degree of Master of Science.

Emine Ülkü Sarıtaş Çukur(Advisor)

Tolga Çukur(Co-Advisor)

Ergin Atalar

Behçet Murat Eyüboğlu

Approved for the Graduate School of Engineering and Science:

Ezhan Karaşan
Director of the Graduate School

ABSTRACT

RAPID MULTI-CONTRAST MAGNETIC RESONANCE IMAGING AND TIME-OF-FLIGHT ANGIOGRAPHY

Toygan Kılıç
M.S. in Electrical and Electronics Engineering
Advisor: Emine Ülkü Sarıtaş Çukur
Co-Advisor: Tolga Çukur
January 2019

Magnetic resonance imaging (MRI) is a frequently used imaging modality for examining soft tissue structures. Long scanning time is the most crucial constraint that limits the use of MRI in the clinics. Partial Fourier (PF), parallel imaging (PI), and compressed sensing (CS) methods have been proposed to accelerate acquisitions by undersampling the data in k-space. However, further increase in acceleration factor as well as image quality are needed in certain applications of MRI, such as T_2-weighted imaging and time-of-flight (TOF) angiography. Previous studies have adopted SPIRiT, a popular CS method, to the problem of multi-contrast image reconstruction. However, the mutual information across different contrast images were not utilized in these studies. In this thesis, a new method is proposed to benefit from the correlated structural information among the images by emphasizing high-spatial frequencies during joint reconstruction. The results obtained from *in vivo* brain scans and numerical phantom show that the proposed method is more robust against parameter selection when compared to conventional methods. For TOF angiography images, the goal of this thesis is to increase the signal-to-noise-ratio and shorten the scanning time, simultaneously. For this purpose, a combination of 2D acceleration in the phase-encode dimensions via CS and 1D PF data acquisition in the frequency-encode dimension to reduce echo time is proposed. Following this data acquisition, a joint reconstruction that iteratively alternates between CS and PF is introduced. *In vivo* angiography results in the brain show that the proposed time-efficient TOF method improves the vessel-background contrast, while decreasing the scanning time.

Keywords: Compressed sensing, joint reconstruction, multi-contrast imaging, T_2-weighted imaging, Time-of-Flight angiography.

ÖZET

HIZLANDIRILMIŞ ÇOKLU-KONTRAST MANYETİK REZONANS GÖRÜNTÜLEME VE UÇUŞ-ZAMANLI ANJİYOGRAFİ

Toygan Kılıç
Elektrik ve Elektronik Mühendisliği, Yüksek Lisans
Tez Danışmanı: Emine Ülkü Sarıtaş Çukur
İkinci Tez Danışmanı: Tolga Çukur
Ocak 2019

Manyetik rezonans görüntüleme (MRG) yumuşak dokuların incelenmesinde sıklıkla kullanılan bir görüntüleme yöntemdir. Çekim sürelerinin uzun olması MRG'nin hastanelerde kullanımını kısıtlayan en önemli etkendir. Veri alımını hızlandırmak için k-uzayını alt örnekleyen kısmi Fourier (KF), paralel görüntüleme (PG) ve sıkıştırılmış algılama (SA) yöntemleri önerilmiştir. Ancak, T_2 ağırlıklı görüntüleme ve uçuş zamanlı (TOF) anjiografi gibi MRG uygulamalarında hızlandırma faktörünün ve görüntü kalitesinin iyileştirilmesine ihtiyaç vardır. Önceki çalışmalar çoklu kontrast görüntü geriçatımı için popüler bir SA yöntemi olan SPIRiT yöntemini benimsemişlerdir. Ancak, bu yöntemlerde farklı kontrastlardaki ortak bilgi, geriçatım aşamasında kullanılmamıştır. Bu tezde, geriçatım sırasında yüksek uzaysal frekansları vurgulayarak görüntüler arasındaki ortak yapısal bilgiden yararlanan yeni bir yöntem önerilmiştir. *In vivo* beyin görüntüleme ve sayısal fantomdan elde edilen sonuçlar, önerilen yöntemin geleneksel yöntemlere kıyasla parametre seçiminde daha gürbüz olduğunu göstermektedir. Bu tezin TOF anjiyografi görüntüleme için amacı, hem sinyal-gürültü oranını artırmak hem de tarama süresini kısaltmaktır. Bu amaçla, faz kodlama yönlerinde SA kullanımı ile iki boyutlu hızlandırma, ve frekans kodlama yönünde bir boyutlu KF veri toplama ile eko zamanı azaltan bir kombinasyon önerilmektedir. Bu veri alımı sonrasında ise SA ve KF yöntemlerini ardışık olarak uygulayan bütünleşik bir geriçatım sunulmaktadır. Beyinde elde edilen *in vivo* anjiyografi sonuçları, önerilen zaman açısından etkin TOF yönteminin, damar-arka plan kontrastını arttırırken tarama zamanını düşürdüğünü göstermektedir.

Anahtar sözcükler: Sıkıştırılmış algılama, bütünleşik geriçatım, çoklu kontrast görüntüleme, T_2 ağırlıklı görüntüleme, uçuş zamanlı anjiografi.

Acknowledgement

In the last three years, I have been fortunate to work with many creative and brilliant people. First, I would like to express my deep gratitude to Emine Ülkü Sarıtaş. I was privileged to be one of her students. She taught me how to preserve my motivation during any study. I believe that this was the most valuable lesson of my master studies, which will help me to be successful throughout life.

I am thankful to my co-advisor Tolga Çukur for following my thesis work closely and supporting me whenever I needed.

I would also like to thank Prof. Dr. Ergin Atalar and Prof. Dr. Behçet Murat Eyüboğlu for giving valuable feedback and being a member of my thesis committee.

I would like to thank the following funding agencies for supporting the work in this thesis: the Scientific and Technological Research Council of Turkey through TUBITAK Grant No 217S069, the Turkish Academy of Sciences through TUBA-GEBIP 2015 program, and the BAGEP Award of the Science Academy.

I am grateful to my lab members: Mustafa Ütkür, Yavuz Muslu, Ali Alper Özaslan, Serhat İlbey, Abdullah Ömer Arol, Ömer Burak Demirel, Damla Sarıca, Çağla Deniz Bahadır, Ahmet Rahmetullah Çağıl, Ecrin Yağız, Ecem Bozkurt, Sevgi Gökçe Kafalı, Semih Kurt, Musa Tunç Arslan, and Mavi Nunn Polatoğlu for influencing my work by their ideas and creativity.

I also want to thank Hulusi Kafalıgönül for accepting me as undergraduate researcher in his group and sharing his invaluable knowledge. Utku Kaya, Zeynep Yıldırım, Ayşenur Karaduman, and Cansu Öğülmüş were not all but some of the precious friends I made along the way.

I would like thank to UMRAM family for their endless support during my master studies. I believe that Umut Gündoğdu, Volkan Açıkel, Aydan Ercingöz, Uğur Yılmaz, Ümit Keleş, Kübra Keskin, Buse Merve Ürgen, Soheil Taraghinia,

Efe Ilıcak, Mohammad Shahdloo, Celal Furkan Şenel, Lütfi Kerem Şenel and many other colleagues made valuable contributions to my work.

I also want to thank ORTANA family for their support, patience and understanding.

Most importantly, I want to thank to my dearest friends Can Mert Yıldız for his support and encouragement, Koray Ertan for his endless patience for my countless questions, Mustafa Ütkür for practical solutions to my problems, Özgür Yılmaz for giving smart advices and Emin Çelik, Ali Alper Özaslan, Salman Ul Hassan Dar, and Ayşe Ecem Bezer for proofreading my writing over and over again.

Finally, I want to thank my beloved family, my father Ali Kılıç, my mother Hatice Kılıç, my brother Arif Samet Kılıç, and his wife Müge Kılıç for always supporting and believing in me.

Contents

List of Figures

List of Tables

Chapter 1

Introduction

Magnetic resonance imaging (MRI) is a widely used modality for detecting the disorders related to soft tissue. The working principle of MRI relies on encoding the magnetization of the hydrogen spins in the human body in frequency domain [1]. It is possible to design different sequences of external magnetic fields to manipulate the magnetization of hydrogen spins. These sequences provide various image contrasts that can be used in the clinical applications of MRI. Turbo-spin-echo (TSE) [2] and time-of-flight (TOF) angiography [3] are two of the popular MRI sequences. TSE sequence is generally used to obtain T_2-weighted MRI images, and TOF sequence is a non-contrast method to acquire angiography images. Although MRI provides flexible image contrast, it has a crucial drawback of prolonged scanning times. One method to reduce scanning time is to increase the number of refocusing radio frequency (RF) pulses to acquire multiple echoes in one repetition time (TR), which is typically long for the TSE sequence. However, the usage of many RF pulses may result in tissue heating, as the sequence pushes the limits of specific absorption rate (SAR) [4]. In addition, the MRI signal experiences significant T_2 decay with multiple refocusing RF pulses. TOF sequence, on the other hand, typically uses short TR values, resulting in relatively short scanning times. Nevertheless, this technique may also have extended scanning times, especially if the region of interest is imaged via a multi-slab acquisition to increase the image quality.

Novel image reconstruction methods were introduced to address the problems mentioned above. Nowadays, parallel imaging techniques such as GRAPPA (Generalized autocalibrating partially parallel acquisitions)[5] and SENSE (Sensitivity encoding)[6] are widely adopted in the clinics to reduce the scanning time. The essence of these methods is to uniformly undersample the k-space. The data acquired from multiple receiver coils, which were previously used for increasing SNR, are then used for filling in the missing k-space data. This idea has then been combined with compressed sensing (CS) methods such as SPIRiT to randomly undersample the k-space, followed by a non-linear image reconstruction [7].

Although these techniques made MRI faster than before, further increase in image quality and acceleration are needed to increase the utility of MRI in the clinics. For this purpose, two different problems were targeted in this study. The first problem is the prolonged scanning time of multiple T_2-weighted image acquisitions. Previously, several solutions were introduced to address this problem [8, 9, 10]. However, these methods did not adequately take into account the mutual information among the multiple T_2-weighted images. Here, I propose a technique that takes advantage of the correlated structural information among the images by emphasizing the high-spatial-frequency content of the k-space data while estimating the SPIRiT kernel.

In the second problem, the focus is on improving the image quality and reducing the scanning time of the TOF angiography sequence. In previous methods, CS [11] and partial k-space data acquisition were performed in the phase-encode direction, which provides high acceleration factors. However, applying the partial k-space acquisition in the readout direction could prove more beneficial as it can decrease the echo time (TE), which in turn increases the contrast between the blood vessels and the background. Here, I propose an iterative technique that alternates between two reconstructions: (1) The partial k-space data in the readout direction are recovered using a projection onto convex sets (POCS) based algorithm [12]. (2) Randomly undersampled k-space data in the phase-encode directions are then reconstructed with the SPIRiT method.

In this thesis, I first present the novel CS technique for multiple T_2-weighted

image acquisition. This technique is demonstrated via numerical phantom simulations and *in vivo* imaging in the brain. The results show that the proposed technique is more robust in the selection of reconstruction parameters compared to the conventional CS methods. Secondly, I present the improved TOF technique via *in vivo* brain imaging results and show that this technique increases image quality while decreasing the scanning time for multi-slab acquisitions.

Chapter 2

Magnetic Resonance Imaging Background

2.1 Principles of MRI

In the presence of an external magnetic field, hydrogen spins in the body precess at a specific frequency, known as the Larmor frequency [13]. This frequency is equal to the strength of the applied magnetic field multiplied by the gyromagnetic ratio of hydrogen. MRI uses this phenomenon to image the distribution of hydrogen spins in the human body, abundant in the form of water and fat. Main magnetic field B_0 is applied to align the randomly oriented magnetic moments of the hydrogen spins, so that a net magnetization is formed. An additional magnetic field called the B_1 field is applied for exciting the hydrogen spins to create the MRI signal. This B_1 field flips the net magnetization to the transverse plane so that the MRI signal can be detected using inductive receive coils. After the spins are excited, their magnetization returns back to the equilibrium state of being aligned with the B_0 field via two different relaxation mechanisms. The first one is the spin-lattice or T_1 relaxation, where the magnetization recovers along the longitudinal direction with a time constant T_1. The second one is called the spin-spin relaxation or T_2 relaxation, caused by the dephasing of the transverse

magnetization after the B_1 field is applied. Different tissues in the human body have different T_1 and T_2 relaxation times, which enables us to obtain MRI images with different contrasts. However, it is still needed to spatially encode the signal. For this purpose, gradient fields are applied along x-, y-, and z-directions [1]. The resulting MRI signal corresponds to the Fourier transform of the underlying spin distribution. In MRI, the data is collected in the spatial frequency domain, which is called the k-space. Taking an inverse Fourier transform of the k-space data yields the MRI image. An illustration of k-space and image domain is shown in Figure 2.1.

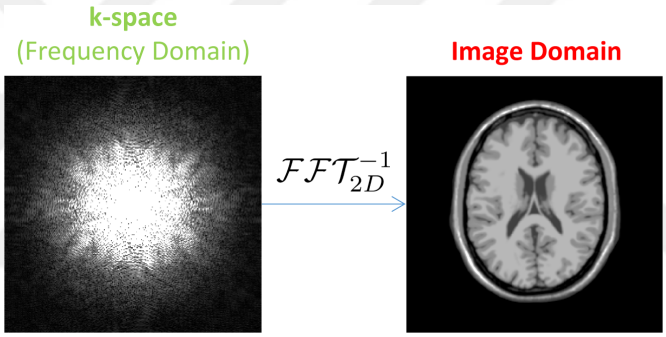

Figure 2.1: After acquiring the k-space data, the MRI image can be obtained by taking the inverse Fourier transform.

2.2 Rapid Imaging Techniques in MRI

This thesis targets multiple T_2-weighted image acquisition and non-contrast angiography. Our goal is to accelerate the data acquisition process and increase the signal level for these applications. The technique proposed in this thesis builds on partial Fourier and compressed sensing methods, which are explained in detail below.

2.2.1 Partial Fourier Reconstruction

MRI images are complex-valued due to off-resonance induced dephasing. If they were real-valued, it would be sufficient to acquire 50% of k-space. Then, the remaining half could be filled with the Hermitian symmetric version of the acquired part. Although MRI images are complex-valued, they typically have a smoothly varying phase in image domain. Hence, acquiring slightly more than half of the k-space is typically sufficient to estimate this low-frequency phase. In partial Fourier reconstruction, the phase of the image is estimated by using the symmetrically acquired part of the center of the k-space. The non-acquired part of the k-space is filled via Hermitian symmetry after removing the estimated phase from the image. This process is called partial Fourier acquisition and reconstruction.

One partial Fourier reconstruction fills the empty part of the k-space based on a projection onto convex sets (POCS) approach [12, 14, 15]. In the equations below, the acquired part of the k-space data in 3D and the symmetrically acquired portion are denoted as $M_{pk}(k_x, k_y, k_z)$ and $M_s(k_x, k_y, k_z)$, respectively. The goal is to fill the unacquired part of the k-space iteratively. Firstly, $M_s(k_x, k_y, k_z)$ is used to estimate the low-frequency phase in image domain, $p(x, y, z)$. Hann windowing can be applied before transformation into the image domain, to prevent potential Gibbs ringing artifacts in the low-resolution image $m_s(x, y, z)$. In Equation 2.1, Hann window is denoted as $H(k_x, k_y, k_z)$. Hence, the slowly varying phase in image domain is obtained as follows:

$$m_s(x, y, z) = \mathcal{F}_{3D}^{-1}\big\{M_s(k_x, k_y, k_z)H(k_x, k_y, k_z)\big\} \tag{2.1}$$

$$p(x, y, z) = e^{i\angle m_s(x,y,z)} \tag{2.2}$$

Next, an initial image is obtained using the acquired data as follows:

$$m_1(x, y, z) = \mathcal{F}_{3D}^{-1}\big\{M_{pk}(k_x, k_y, k_z)\big\} \tag{2.3}$$

The image phase in each iteration is forced to the estimated low-resolution phase:

$$m_{i,pc}(x, y, z) =\mid m_i(x, y, z) \mid p(x, y, z) \tag{2.4}$$

This phase-constrained image, $m_{i,pc}(x, y, z)$, is transformed to k-space by Fourier transform to obtain $M_{i,pc}$. The portion that corresponds to the acquired part of the k-space is replaced with the actual acquired data from M_{pk} to provide data consistency. The image in the next iteration, $m_{i+1}(x, y, z)$, is obtained by taking Fourier transform of the resulting k-space data.

Note that, the acceleration factor for the partial Fourier method has an upper limit of 2. As explained in the next section, parallel imaging techniques can yield much higher acceleration factors.

2.2.2 Parallel Imaging

Multiple coils are typically used to collect MRI data, which helps to increase SNR. In addition, the spatially varying sensitivities of the receive coils can be used to accelerate image acquisition. An illustration of multi-coil image acquisition is demonstrated in Figure 2.2. There are numerous acceleration methods that exploit the simultaneous use of multiple receive coils [6, 5, 16]. Among these methods, Generalized Autocalibrating Partial Parallel Acquisition (GRAPPA) is the most popular and widely used technique.

The GRAPPA framework performs its algorithm in k-space. Acceleration factor in MRI can be determined according to the ratio between the total number of samples of k-space lines and acquired number of k-space lines. The algorithm uniformly undersamples the k-space in the phase-encode directions, followed by an interpolation of the unacquired data. The interpolation kernel in this step is estimated from the fully sampled central region in k-space.

An example sampling scheme and flowchart of the method is given in Figure 2.3. In this specific example, the k-space is undersampled in both k_y and k_z phase-encoding direction. The central region is fully sampled to estimate the interpolation kernel. While estimating the kernel, both inter-coil and intra-coil neighborhood information are used. Using this strategy, the following linear

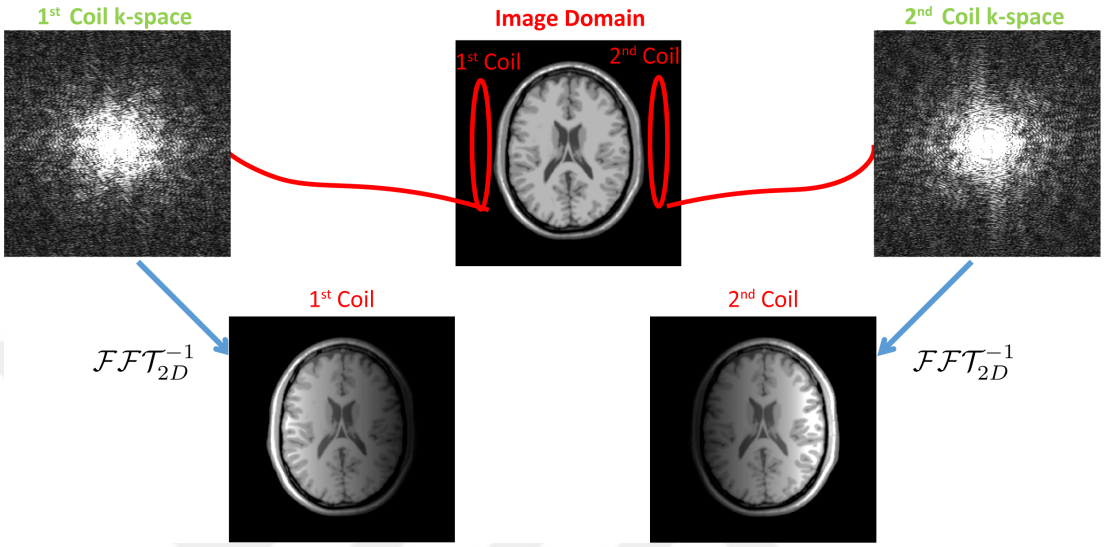

Figure 2.2: Multi-coil image acquisition. The image from each coil corresponds to the full MRI image multiplied by the sensitivity map of that coil.

equation is formed:

$$s_k = A_k g_k \tag{2.5}$$

where k is the sampling strategy index (see Fig.2.3), A_k is the neighborhood data taken from all coils for sampling strategy k, g_k is the corresponding kernel containing the weights between acquired and unacquired data, and s_k is the synthesis data from the calibration region. The kernel weights are estimated in a regularized fashion using the following expression:

$$g_k = (A_k^* A_k + \beta I)^{-1} A_k^* s_k \tag{2.6}$$

Here, β is the Tikhonov regularization parameter. This operation is repeated for all coils and for different sampling strategies, as illustrated in Figure 2.3. The main advantage of the GRAPPA technique is that it synthesizes the k-space data for all coils, as opposed to image domain parallel imaging algorithms that only yield a single combined image. In addition, it is more robust against subject motion. However, the acceleration factor in parallel imaging techniques are limited by a coil geometry dependent noise amplification, quantified by the g-factor [17]. The next section describes compressed sensing, which can achieve higher acceleration factors when compared to parallel imaging methods.

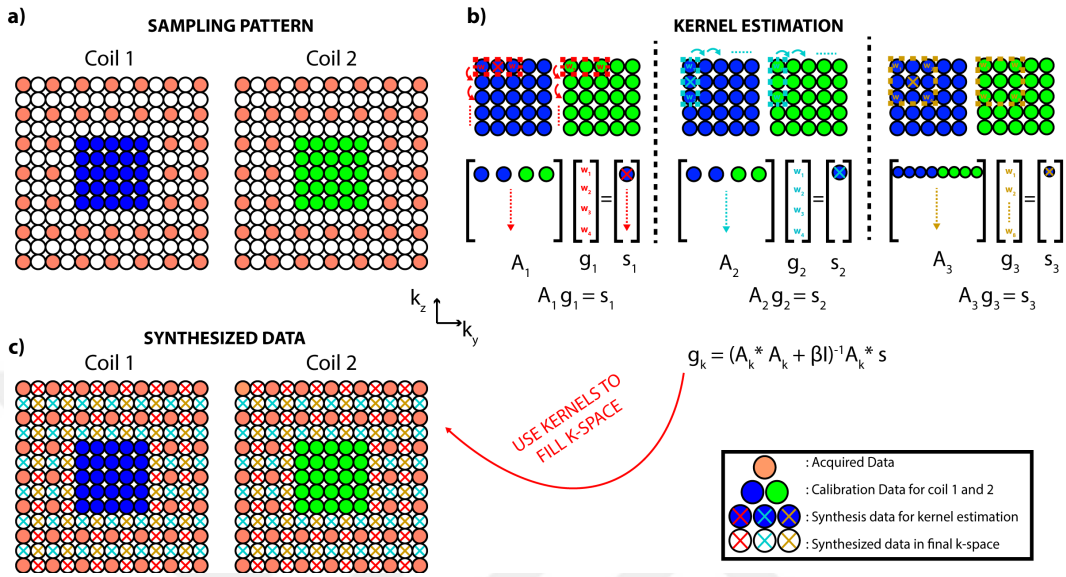

Figure 2.3: Flowchart of GRAPPA method a) Sampling pattern in k-space. In this toy example, 13×13 k-space and 5×5 calibration region are used. These calibration regions are demonstrated with blue and green for coil 1 and coil 2, respectively. b) Because of the sampling strategy, 3 different kernels are estimated in a regularized fashion. These different kernels are denoted with red, cyan, and gold colors, shown here for the cause of coil 1. c) Using the estimated kernels from the calibration region, the unacquired k-space points are filled by interpolating the nearby acquired k-space data points.

2.2.3 Compressed Sensing (CS)

CS theory indicates that it is possible to reconstruct signals without obeying Nyquist theorem, if the following 3 requirements are satisfied [11]:

- Transform sparsity
- Incoherent undersampling
- Non-linear reconstruction

Transform sparsity means that the acquired signal should have a sparse representation in a known domain other than the sampling domain. A domain can be called "sparse" if a significant portion of the pixels are zeros. In MRI, Wavelet

domain is one of the most commonly used domain to enforce transform sparsity. As illustrated in Figure 2.4 a, most of the pixels in the Wavelet domain representation of MRI images are zero or have values very close to zero.

Incoherent undersampling is another requirement for compressed sensing. Uniform undersampling of k-space data can create coherent aliasing artifacts. In contrast, a random undersampling of k-space yields incoherent (noise-like) artifacts in the sparsifying transform domain. One example for incoherent undersampling of k-space is demonstrated in Figure 2.4 b.

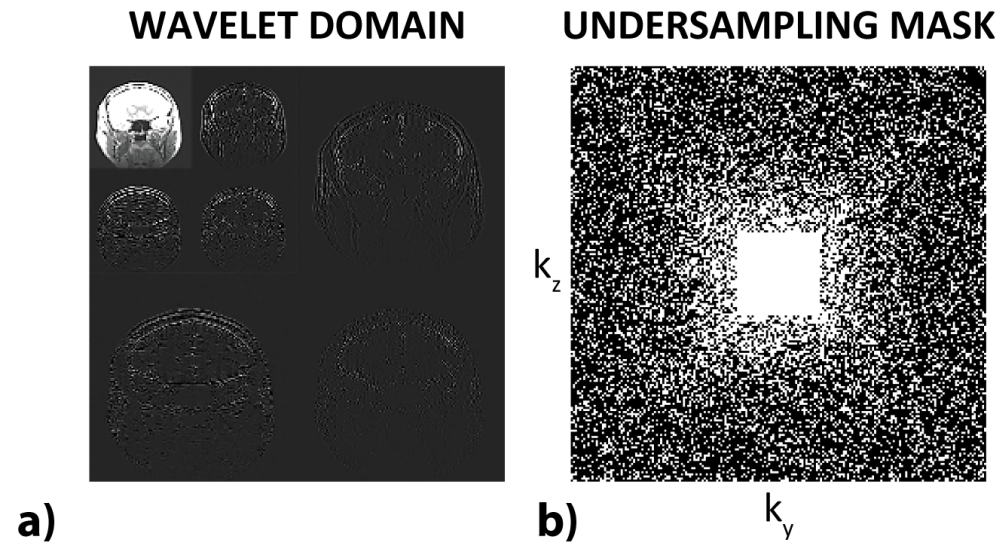

Figure 2.4: a) Wavelet domain representation of an MRI image. This representation is sparse, as most of the pixels in Wavelet domain are zero or have values very close to zero. b) Random undersampling of k-space. The central part of the k-space is fully sampled, whereas the sampling density decreases at high-spatial-frequency regions.

After incoherent undersampling, a *non-linear reconstruction* must be utilized to reconstruct the images, enforcing both transform sparsity and data consistency. This procedure basically eliminates the noise-like artifacts in the image domain, iteratively.

The SPIRiT framework is a popular application of compressed sensing [7]. Following the incoherent sampling requirement, SPIRiT applies a pseudo-random undersampling in the k-space, where the probability density function for the

undersampling mask decreases at higher spatial frequencies (see 2.4 b). On the image reconstruction side, it uses a similar interpolation formalization as in GRAPPA, with one difference: SPIRiT estimates only one interpolation kernel, as demonstrated in Fig.2.5, which also demonstrates the kernel estimation scheme for SPIRiT. Estimated kernel weights in Eq 2.6 are reordered such that they correspond to a convolution operation in a matrix form, G [7]. After the kernel is estimated, the following optimization problem is solved to reconstruct the k-space data:

$$\arg\min_{x} \|(G-I)x + (G-I)y\|_2^2 + \lambda \|x\|_2^2 \tag{2.7}$$

Here, x and y are the unacquired data to be recovered and acquired k-space data, respectively. In Eq. 2.7, the first term shows the calibration consistency and the second term shows the data consistency. In addition, an ℓ_2 regularization term with weight λ is used to penalize the energy of the reconstructed k-space data.

2.3 Targeted Applications

2.3.1 T_2-Weighted MRI Data Acquisition

In MRI, there are different sequences for achieving T_2-weighted contrast. Spin-echo sequences with long TR and medium TE can be used for this purpose [18]. While long TR is used to decrease possible T_1-weighting effects, it causes prolonged scanning times. This problem can be alleviated by taking multiple echoes in one TR [2]. Multiple 180° RF pulses are performed to obtain these echoes. This method is called Turbo Spin Echo (TSE) and the number of RF pulses in one repetition is called the turbo factor. Typical numbers for turbo factor range between 12 and 30 [4]. Although TSE is widely used, it has some limitations. SAR values increases with the number of RF pulses and their flip angles. When it comes to 3D imaging, it is not practical to use TSE for T_2-weighted imaging, due to the additional phase-encoding direction that once again increases the scanning time. Variable flip angle concept is introduced to solve this problem [19]. The

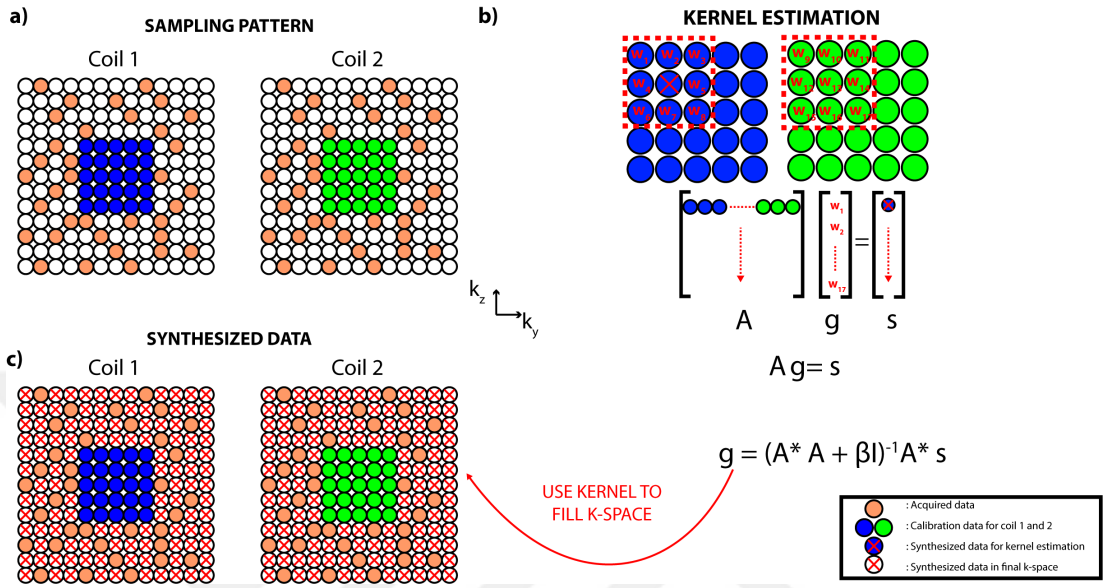

Figure 2.5: Flowchart of SPIRiT. a) Sampling pattern in k-space. In this toy example, 13×13 k-space and 5×5 calibration region are used. The calibration region in k-space is demonstrated with blue and green for two coil 1 and coil 2, respectively. b) Unlike the GRAPPA method, only one kernel is estimated in SPIRiT. In addition to this, kernel weights are computed using all neighborhoods without considering the sampling pattern. This makes SPIRiT suitable for any sampling strategy. c) The synthesized data can be obtained by applying the kernel weights for interpolating the k-space data.

essence of variable flip angle concept is grounded in usage of the low flip angle RF pulse train instead of 180° RF pulses. The transverse magnetization could reach a steady state using these low flip angle RF pulses. This steady state is called pseudo-steady state (PSS), because it is temporary due to T_1 and T_2 relaxation [20]. The sequences benefiting from variable flip angle concept applies higher flip angle RF pulses to the center of the k-space rather than the peripheral regions, which have lower SNR. Therefore, transmitted RF energy to subject is drastically decreased while the signal level in the center of the k-space is preserved. Up to 200 echoes can be reached using variable flip angle concept at 3T MRI machine.

While applying the aforementioned methods yield practical scanning times for a single T_2-weighted image, multi-contrast 3D T_2-weighted image acquisitions still need further accelerations. Example T_2-weighted images with different echo times are shown in Figure 2.6.

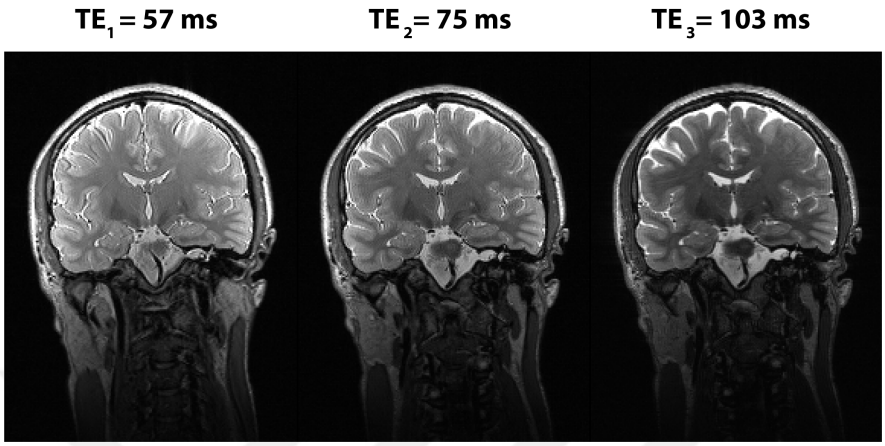

Figure 2.6: Multiple T_2-weighted coronal images with different echo times are for a healthy subject.

2.3.2 Time-of-Flight Angiography

Time-of-flight (TOF) angiography is broadly used in non-contrast-enhanced evaluations of intracranial vasculature. The goal in this method is to increase the contrast between the stationary background and the flow related non-stationary signals. Stationary tissues are saturated in the case of short repetition time. On the other hand, blood has regular flow and is not affected by short TR. In addition, shortening the TE also increases the signal coming from blood because of capturing the signal before diminished. To enhance inflow effects while maintaining high signal-to-noise ratio (SNR), multi-slab 3D acquisitions are commonly preferred. However, this comes at the cost of prolonged scan times. Maximum intensity projection (MIP) operation is performed to visualize the vessels in 2D plane. This operation computes the maximum values in the desired direction and maps it to a 2D plane. An example is shown in Figure 2.7 for different slices of TOF images and the corresponding MIP image.

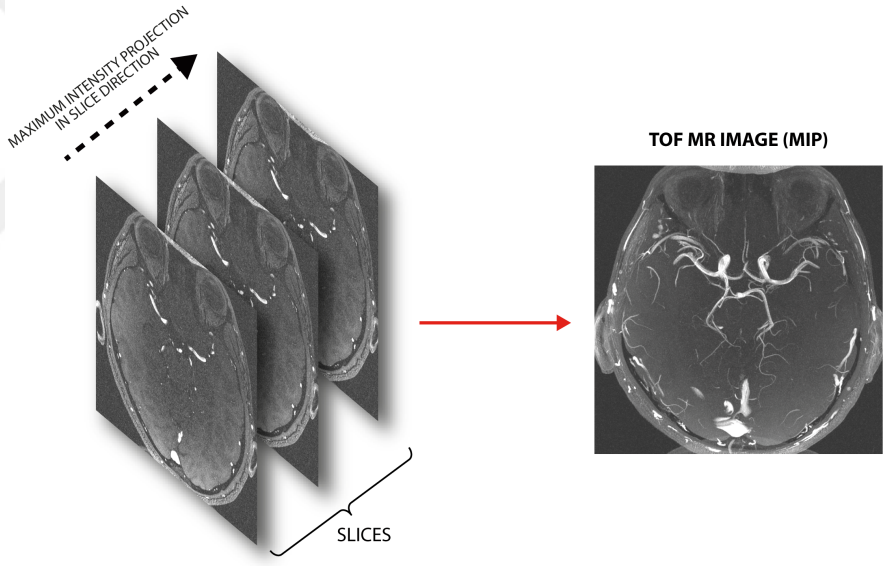

Figure 2.7: Multiple slices for TOF images and the corresponding Maximum intensity projection (MIP).

Chapter 3

Joint Multi-contrast Reconstruction of T_2-Weighted Images by Filtered Kernel Estimation

3.1 Introduction

T_2 relaxation time is very crucial for differentiating between normal and pathological tissues. A linear correlation between water content and T_2 relaxation time was found in previous studies [21]. Since tumor tissues have high water content, it makes T_2 relaxation time a good candidate for the detection of abnormal tissues [22, 23, 24]. It is important to increase the contrast between normal and pathological tissues to distinguish them. For T_2-weighted imaging, this contrast is directly related to echo time (TE). Acquiring multiple T_2-weighted images with different TE values can facilitate the detection of diseased tissues [22]. In addition, T_2 relaxation time can be calculated from multiple T_2-weighted images, which can further help to identify the disease [25]. However, prolonged scanning time is a problem for acquiring multiple T_2-weighted images in clinical use, especially for

3D imaging. To increase the scan efficiency, accelerated image acquisition can be performed, where it is essential to successfully recover the missing data.

One strategy to recover the missing data is to perform individual reconstructions of each undersampled T_2-weighted acquisition. Parallel imaging and compressed sensing are popular and clinically used techniques for recovering the missing points. SENSE is an image domain parallel imaging method to reconstruct images using coil sensitivities [6]. However, this framework requires additional scanning to obtain coil sensitivities, which makes the reconstruction sensitive to subject motion. On the other hand, GRAPPA is a k-space based auto-calibrated parallel imaging method, which estimates an interpolation kernel from the fully sampled k-space region, as explained in Chapter 2.2.2 [5]. However, GRAPPA has limited acceleration capabilities because of geometry dependent noise amplification. Besides these techniques, CS methods propose higher acceleration factors using random undersampling [11]. However, using these methods individually for each image ignores the correlated structural information among multiple T_2-weighted images.

An alternative strategy is to jointly reconstruct multi-echo acquisitions to better utilize correlated information. Some of the previously proposed multi-contrast reconstruction methods estimate the interpolation kernel from the acquired calibration regions from all contrasts [26, 27, 28, 29, 30, 31, 33]. SPIRiT kernel was adapted for the reconstruction of multi-contrast data in some of these methods [26, 27, 28, 32]. Besides these explicit methods, joint sparsity terms were used to exploit common features between different contrasts [9]. A Bayesian CS method, which utilizes sparsity in gradient domain, was also proposed to perform multi-contrast imaging [8]. Some of the above-mentioned multi-contrast methods directly target the multi-echo T2-weighted image reconstruction problem [34, 35, 10]. However, all these methods neglect the fact that images share more similarities at higher frequencies compared to lower frequencies.

This thesis proposes to jointly reconstruct multiple T_2-weighted images using a modified SPIRiT framework. To utilize correlated information between multiple echoes, the calibration region is first filtered to give more weight to the shared

information at higher spatial frequencies. This process results in a more optimal kernel estimation. In the reconstruction step, this optimized kernel is used to synthesize the images from undersampled data. Comprehensive simulations and *in vivo* results demonstrate that the proposed method is significantly more robust to changes in parameters that require tuning, such as the iteration number and regularization parameters, when compared to conventional SPIRiT.

3.2 Methods

In the proposed method, the goal is to improve SPIRiT kernel estimation step for multi-contrast acquisitions. As described in Chapter 2.2.3, in the conventional SPIRiT method, interpolation kernel is computed from the calibration region from multi-coil data. Missing points in the k-space are filled by the interpolation kernel using weighted linear combination of acquired data. Such interpolation operation is well-suited for multi-coil data, because spatially close regions in the image domain are structurally similar in both low and high frequencies. However, in multi-contrast acquisitions a higher degree of similarity is observed in tissue boundaries captured by high spatial frequencies whereas image contrast itself or tissue signal levels themselves can show dissimilarity as captured by low spatial frequencies. This dissimilarity makes the SPIRiT kernel estimation suboptimal for multi-contrast data. Therefore, the proposed method aims to improve kernel estimation by more heavily weighting high spatial frequencies in contrast to low spatial frequencies by applying high-pass filtering.

3.2.1 Interpolation Kernel

In the conventional SPIRiT method, the interpolation kernel across multiple coils is computed from the calibration region. Previous attempts in adapting SPIRiT to multi-contrast reconstructions directly use this approach, as well. Accordingly, separate acquisitions in multi-contrast data are treated as separate channels in the interpolation kernel. Without loss of generality, in a 3D cartesian acquisition

there is 2D undersampling. Inverse Fourier transformation is taken along the readout direction to reduce computational complexity [36]:

$$Y^c\left(x, k_y, k_z\right) = \mathcal{F}_x^{-1}\left\{Y^c\left(k_x, k_y, k_z\right)\right\} \tag{3.1}$$

Here, $Y^c\left(x, k_y, k_z\right)$ are hybrid k-space undersampled data, which have $N_y \times N_z$ phase-encode samples and N_x readout samples, k_x is the k-space readout index, k_y and k_z are the k-space phase-encode indexes, and x is the image domain readout index, $\mathcal{F}_x^{-1}$ is the 1D inverse Fourier transform in the readout direction, c is the contrast index at total of N_c contrasts. Here, $Y_x^c = Y^c(x, k_y, k_z)$ is used to denote readout cross section from the 3D hybrid data in this section. A calibration matrix is constructed by reordering the calibration region of size $m_y \times m_z$ selected from the k-space data, Y_x^c:

$$A_x^c = \mathcal{T}\left\{Y_x^c\right\} \tag{3.2}$$

where A_x^c is a $(m_y - n_y + 1) \cdot (m_z - n_z + 1) \times (n_y \cdot n_z \cdot N_c - 1)$ matrix; n_y and n_z denote the kernel sizes, $\mathcal{T}$ is a transformation operator that performs reordering. Kernel estimation can then be cast as a linear system of equations in the following form,

$$s_x^c = A_x^c g_x^c \tag{3.3}$$

where s_x^c is synthesized data and g_x^c represents the kernel weights. These weights reflect the linear relationship between a target k-space sample and its neighbors across all contrasts with length $n_y \cdot n_z \cdot N_c - 1$ for kernel size of $n_y \times n_z$. The above equation is solved using the pseudo-inverse operation, i.e.,

$$g_x^c = \left(A_x^{c^*} A_x^c + \beta I\right)^{-1} A_x^c s_x^c \tag{3.4}$$

where β is a regularization weight, which facilitates matrix conditioning and noise resilience [32], and I is the identity matrix. This process is illustrated in Figure 3.1a.

In the proposed method, the calibration region is high-pass filtered to emphasize the structural similarities at high spatial frequencies among multi-contrast

data:

$$H(k_r) = \begin{cases} \sigma & \text{if } 0 < k_r < k_{stopband} \\ \sigma + (1-\sigma)\sin^2\left(\frac{2\pi(k_r - k_{stopband})}{4w}\right) & \text{if } k_{stopband} < k_r < k_{passband} \\ 1 & \text{if } k_r > k_{passband} \end{cases} \quad (3.5)$$

where,

$$k_r = \sqrt{\left(\frac{2k_x}{N_x}\right)^2 + \left(\frac{2k_y}{N_y}\right)^2 + \left(\frac{2k_z}{N_z}\right)^2} \quad (3.6)$$

Here, σ is a small non-zero number that suppresses low-spatial frequencies, k_r denotes the normalized k-space radius, $k_{stopband}$ and $k_{passband}$ define the passband and the stopband edge points of the high-pass filter, respectively. The user specified parameters σ, $k_{stopband}$, and $k_{passband}$ vary in the range $[0, 1]$. The transition region of the filter, i.e. the difference between the passband and the stopband regions of the highpass filter, is defined as $w = k_{passband} - k_{stopband}$. In the proposed method, the calibration matrix is obtained from reordering the high-pass filtered calibration region:

$$A^c_{x(hp)} = \mathcal{T}\left\{\mathcal{F}_x^{-1}\left\{Y^c\left(k_x, k_y, k_z\right) H\left(k_x, k_y, k_z\right)\right\}\right\} \quad (3.7)$$

where $A^c_{x,(hp)}$ is the calibration matrix. The respective kernel weights, $g^c_{x,(hp)}$, are then obtained via the following operation:

$$g^c_{x(hp)} = \left(A^{c*}_{x(hp)} A^c_{x(hp)} + \beta I\right)^{-1} A^c_{x(hp)} s^c_{x(hp)} \quad (3.8)$$

where $s^c_{x,(hp)}$ are the synthesized data. A flowchart of the proposed method is demonstrated in Figure 3.1 b.

3.2.2 Undersampling Patterns and Kernel Estimation

3D cartesian data were undersampled with isotropic acceleration in the two phase-encode directions for both numerical phantom and *in vivo* data. Variable-density random undersampling was used to achieve an acceleration factor of $R = 3$. [11] Random undersampling patterns were created using probability density functions

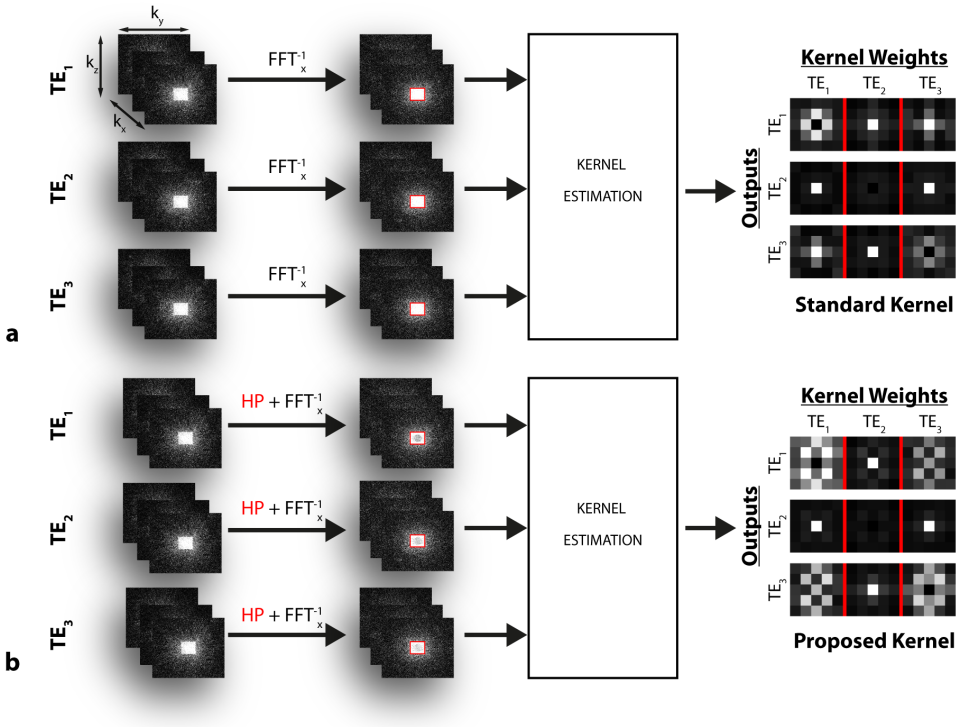

Figure 3.1: Flowcharts of conventional SPIRiT and the proposed method. a) Firstly, 1D IFFT is applied in readout dimension for different contrasts to transform 3D problem into 2D problems. The same readout sample is selected from hybrid 3D data for each contrast. Calibration region is denoted using red rectangles in the figure. The kernel estimation is performed using this calibration treating each contrast as a separate channel. Sample kernel weights for each output are shown. b) In the proposed method, the main difference is that a high-pass filter is applied before 1D inverse Fourier transform to highlight the intermediate frequencies in the kernel estimation step. This is evident in the sample kernels shown on the right. In the 5×5 kernels, it is clear that higher weights are assigned to pixels at higher spatial frequencies for the proposed method compared to conventional SPIRiT. This shows that the proposed method puts greater emphasis on high frequencies.

(PDFs), which were fully-sampled in low-frequencies for kernel estimation. Sampling probability decreased towards high frequencies with polynomial of degree $p = 5$. Calibration regions of size 86×72 and 44×38 were used for numerical phantom and *in vivo* data, respectively. These calibration regions corresponded to nearly 20% of k-space. A Monte-Carlo procedure was deployed to select final sampling patterns with minimal aliasing energy. For this purpose, 1000 candidate patterns were generated. The maximum of the sidelobe-to-peak ratio (SPR) was calculated from candidate patterns' point spread functions (PSF), and a pattern that minimize the SPR was selected. Disjoint patterns were used for separate contrasts to increase aggregate k-space coverage [31]. Different kernel sizes, which are 5×5, 7×7, 9×9 and 11×11, were tested. It was observed that 5×5 kernel performed well in both phantom and *in vivo* data. Filter parameters $k_{stopband}$ and $k_{passband}$ were varied among the following pairs: [0.05,0.15], [0.05,0.2], [0.1,0.15], [0.1,0.2]. It was observed that [0.1 0.2] outperform the remaining parameter values. The suppression parameter σ was also evaluated at $\{0, 0.3, 0.5, 0.7\}$. Higher values of σ yielded degraded performance, hence, σ was selected as 0.

3.2.3 Reconstruction Methods

The system of equations given in Eq. 3.2 and 3.7 were expressed in matrix form for convenience. The kernels obtained in Eq. 3.4 and 3.8 were reordered such that G_x for SPIRiT and $G_{x,(hp)}$ for SPIRiT$_{\text{hp}}$ correspond to convolution operation in a matrix form (also see Eq. 2.2.3).

The comparison methods and SPIRiT$_{\text{hp}}$ are explained in detail in the following sections:

- **Zero-fill (ZF)**: Reconstructions were obtained from direct inverse Fourier transform of undersampled k-space for comparison purposes.
- **SPIRiT**: The calibration consistency is enforced by the following expression:

$$t_x = G_x t_x \tag{3.9}$$

where t_x is the entire 2D hybrid grid samples for all contrasts. Then, an optimization problem was formulated, which enforced consistency between the acquired data and the calibration consistency:

$$\arg\min_{t_x} \|(G_x - I)t_x + (G_x - I)y_x\|_2^2 + \lambda \|t_x\|_2^2 \tag{3.10}$$

Here, y_x presents the acquired data. In this formalization, the terms t_x and y_x are separated so that reconstruction does not change the acquired samples. An ℓ_2-regularization term with weight λ was used to penalize the energy in recovered k-space samples. The regularization weight λ was varied in the range $(0.001, 1]$ and the reconstruction performance was evaluated using peak-signal-to-noise ratio (PSNR). Except for extreme values, it is observed that this weight does not affect PSNR results. Hence, $\lambda = 0.01$ was selected as the optimized value. Using these parameters, the optimization problem was solved using the iterative least squares (LSQR) method [37].

- **SPIRiT$_{\mathbf{hp}}$**: Our proposed method changes the calibration consistency part by applying the kernel that is obtained from filtered calibration regions. Similar to the SPIRiT method, the proposed method enforced the calibration consistency by the following operation:

$$t_x = G_{x,(hp)} t_x \tag{3.11}$$

Then, the following optimization problem was solved to find the k-space values.

$$\arg\min_{t_x} \left\|(G_{x,(hp)} - I)t_x + (G_{x,(hp)} - I)y_x\right\|_2^2 + \lambda \|t_x\|_2^2 \tag{3.12}$$

The same parameters as in the SPIRiT method were used for solving this optimization problem.

Libraries in SPIRiT toolbox were used for implementing the proposed method [7]. All reconstruction algorithms were performed in MATLAB 2015b (The MathWorks, Natick, MA).

3.2.4 Numerical Phantom

Numerical phantoms were simulated for three T_2-weighted spin echo acquisitions at TE = 10, 30, 50 ms, TR = 6000 ms, matrix size 434×362×88 (phase×slice×readout), 90° flip angle; 0.5 mm isotropic resolution (http://www.bic.mni.mcgill.ca/brainweb). The following set of tissue parameters were employed: T_1/T_2 of 2569/329 ms for cerebrospinal fluid (CSF), 833/83 ms for gray matter, 500/70 ms for white matter, 350/70 ms for fat, and for 900/47 ms muscle [38].

Reconstructions for SPIRiT and the proposed method were obtained for regularization parameters in the range $\beta \in [0.001, 0.1)$ with a step size of 0.002, and iteration numbers in the range $[1, 70]$ with a step size of 5. In addition, ZF reconstructions were implemented for comparison. Images were normalized according to 95^{th} percentile of image intensities to avoid possible image scale differences. PSNR was used to assess image quality of the proposed method, SPIRiT, and ZF. The optimum regularization parameter for each contrast was first determined independently from yielding the maximum PSNR and then averaged across contrasts to calculate the final parameter value. 95% of the final value was prescribed for representative images to prevent over-regularization. Once the optimum regularization parameter was selected, PSNR was averaged across contrasts and the number of iterations that yielded the maximum PSNR was selected. Then, SPIRiT and the proposed method images for the optimum parameters were compared via error maps. In addition, the reconstructed images at iteration number 5, 15, 30, and 45 at TE = 10 ms were compared for optimum Tikhonov regularization parameter for both SPIRiT and the proposed method.

3.2.5 *In Vivo* Experiments

In vivo experiments were conducted on two healthy subjects with 3D SPACE (Sampling Perfection with Application optimized Contrasts by using different flip angle Evolutions) [39] sequence on a 3T scanner (Magnetom Trio A Tim,

Siemens) using a 32-channel head coil. Variable flip angle scheme was selected for T_2-weighted acquisitions. Three different TE values were used: TE = 145 ms, 257 ms and 320 ms (corresponding to effective TE values of TE_{eff} = 57 ms, 89 ms, and 103 ms, respectively). The images were registered by taking the first scan as reference in FSL [40]. Adaptive combination across coils was applied to preserve phase [41]. Other scan parameters were: coronal orientation, FOV_{read} = 256 mm, FOV_{phase} = 192 mm; TR = 3000 ms , voxel size = 1×1×1 mm^3 , matrix size = 256×193×224 (readout×phase×slice), scan time = 11 min 14 sec, readout bandwidth of 781 Hz/Px. An A/P and R/L phase-encode dimensions and S/I readout dimension were used. Experimental procedures were approved by the local ethics committee and written informed consent was taken from all participants.

Fully sampled acquisitions were retrospectively undersampled. Images were reconstructed with SPIRiT and the proposed method for T_2-weighted acquisitions at TE_{eff} = 57, 89, and 103 ms. Regularization parameters were examined in the range $\beta \in [0.001, 0.1)$ with a step size of 0.002, and iteration numbers in the range $[1, 70]$ with a step size of 5. In addition, ZF reconstructions were implemented for comparison. As done for the numerical phantom case, images were normalized according to 95^{th} percentile of image intensities. Optimum regularization parameters were selected following the procedure described for the numerical phantom case.

Then, reconstruction results at the optimum parameter values were compared with error maps. In addition, the reconstructed images at iteration numbers 5, 15, 30, and 45 at TE_{eff} = 57 ms were compared for optimum Tikhonov regularization parameter for both SPIRiT and the proposed method.

3.3 Results

3.3.1 Numerical Phantom Results

The proposed method was first demonstrated on the numerical brain phantom. Figure 3.2 shows the PSNR maps for reconstructions obtained by SPIRiT and the proposed method as a function of iteration number and β. Per iteration, each reconstruction took approximately 0.2 seconds for both methods. From these maps, optimum iteration numbers were found to be 20 for SPIRiT and 45 for SPIRiT$_{\text{hp}}$. Optimum Tikhonov regularization parameters were found to be 0.067 for SPIRiT and 0.095 for SPIRiT$_{\text{hp}}$. PSNR maps indicate that SPIRiT works well in a very narrow region and its performance degrades when the iteration number increases. In contrast, PSNR values for the proposed method are near-optimal across a broad range and less dependent on changes in iteration number. This argument is quantitatively evaluated for three situations: (1) The average PSNR value across the entire map is 26.85 ± 0.54 dB for SPIRiT and 29.00 ± 1.19 dB for SPIRiT$_{\text{hp}}$ (mean $\pm$ SD across contrasts). (2) The average PSNR across the map for optimized Tikhonov parameter is 26.52 ± 0.60 dB for SPIRiT and 29.85 ± 1.29 dB for SPIRiT$_{\text{hp}}$ (3) The average PSNR value for the optimum iteration numbers are 28.35 ± 0.76 dB for SPIRiT and 29.88 ± 1.28 dB for SPIRiT$_{\text{hp}}$. Note that, the conventional ZF reconstructions yield an average PSNR value of 23.75 ± 0.45dB.

Figure 3.3 shows the representative reconstructions using ZF, SPIRiT, and the proposed method. Absolute error maps are shown for SPIRiT and the proposed method. For these images, SPIRiT improves PSNR by 4.94 ± 1.12 dB over ZF and the proposed method improves PSNR by 7.14 ± 1.00 dB (mean $\pm$ SD average for TE = 10, 30, and 50 ms). It is expected that the proposed kernel would be sensitive to correlated information across contrasts because low spatial frequencies are down-weighted. Therefore, tissue boundaries that are captured by high-frequencies are better reconstructed. As a result, proposed error levels are lower than SPIRiT at all echo times. Errors in high frequency textures are lower for the proposed method, especially for TE = 50 ms, which has higher spatial frequency content due to enhanced contrast between gray matter and cerebrospinal

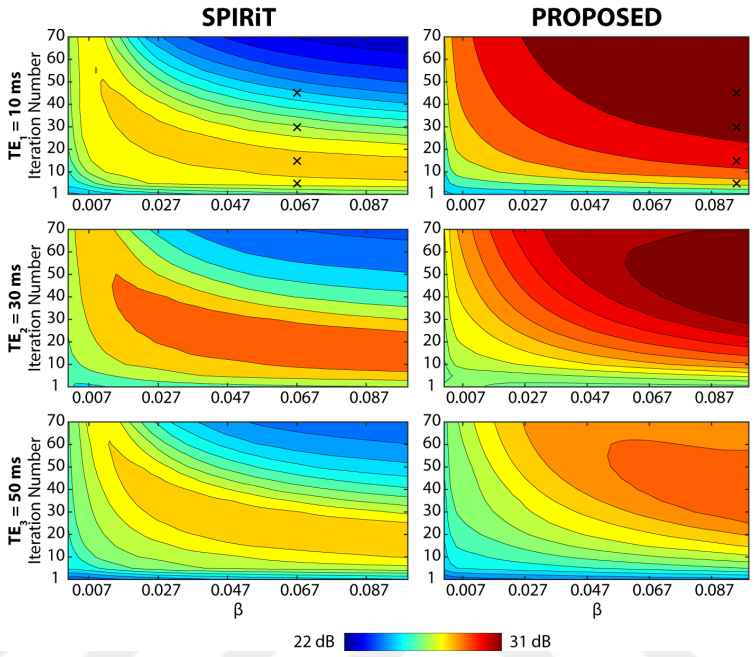

Figure 3.2: Quantitative comparison of reconstructions obtained by SPIRiT and the proposed method for the numerical brain phantom in the range of iterations between 1-70, and Tikhonov regularization parameter β between 0.001-0.1. PSNR maps for three different contrasts with TE = 10, 30, and 50 ms are demonstrated. All contour plots are shown on the same scale to enable comparison between methods and across contrasts.These results show that the proposed method outperforms SPIRiT, especially when robustness against iteration number is considered. Black cross signs mark iterations 5, 15, 30, and 45, with the corresponding reconstructed images shown in Fig. 3.4

fluid.

Figure 3.4 shows the reconstructions of the numerical phantom at multiple distinct iteration numbers for SPIRiT and SPIRiT$_{\text{hp}}$ for TE = 10 ms. Following iteration numbers are shown to test the reliability of each method against changes in iteration number: 5, 15, 30, and 45. If we have a perfect kernel estimate, applying more iterations during the reconstruction should not alter the reconstructed images. However, it is observed that SPIRiT causes increasing noise amplification towards higher iteration numbers. In contrast, proposed method is more robust, because kernel estimation is performed after filtering out dissimilar information across images. PSNR comparison confirms the visual inspection (see Table 3.1). The proposed method improves PSNR by 3.50 ± 2.72 dB over SPIRiT (mean $\pm$

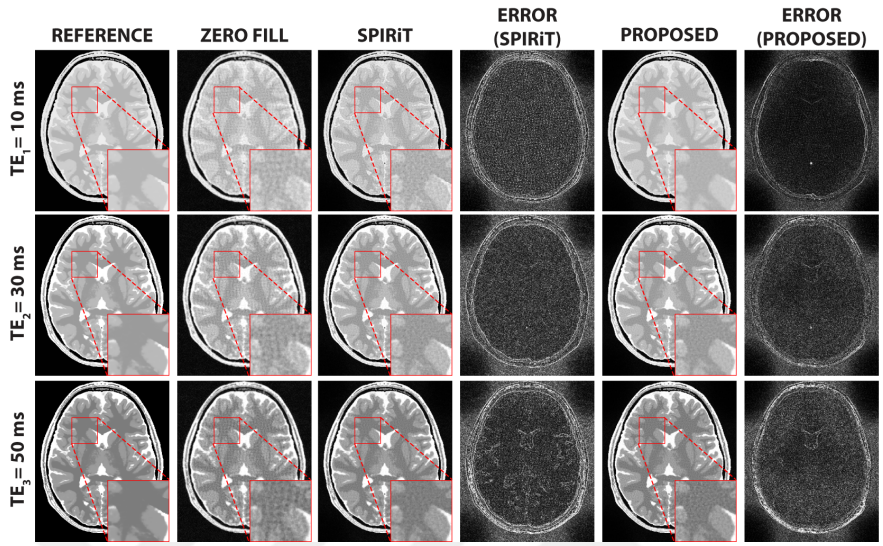

Figure 3.3: Representative results from the numerical brain phantom, showing the reconstructed T_2-weighted images with different echo times (TE = 10, 30, and 50 ms). Reconstruction and zoom-in versions of reference, zero fill method, SPIRiT, and the proposed method are demonstrated for R = 3 acceleration. Absolute error plots with 3 times amplification are shown for SPIRiT and the proposed method to emphasize the differences. For the first contrast, it is observed that SPIRiT could not eliminate noise coming from the random sampling properly. High frequency content corresponding to tissue boundaries are better captured by the proposed method for all three contrasts, especially for TE = 50 ms.

SD average across iterations).

3.3.2 *In Vivo* Results

In vivo T_2-weighted brain images using three different echo times were acquired. Reconstructions obtained by SPIRiT and the proposed method were evaluated at various βs and number of iterations. Per iteration, each reconstruction took approximately 0.1 seconds for both methods. Figure 3.5 demonstrates the obtained PSNR values for a representative subject. For these PSNR values, the optimum Tikhonov regularization parameters are 0.095 for SPIRiT and 0.093 for $\text{SPIRiT}_{\text{hp}}$. Optimum iteration numbers are 10 for SPIRiT and 15 for $\text{SPIRiT}_{\text{hp}}$. Although the SPIRiT shows close results for the optimum Tikhonov regularization parameter and number of iterations, general evaluation of PSNR maps show

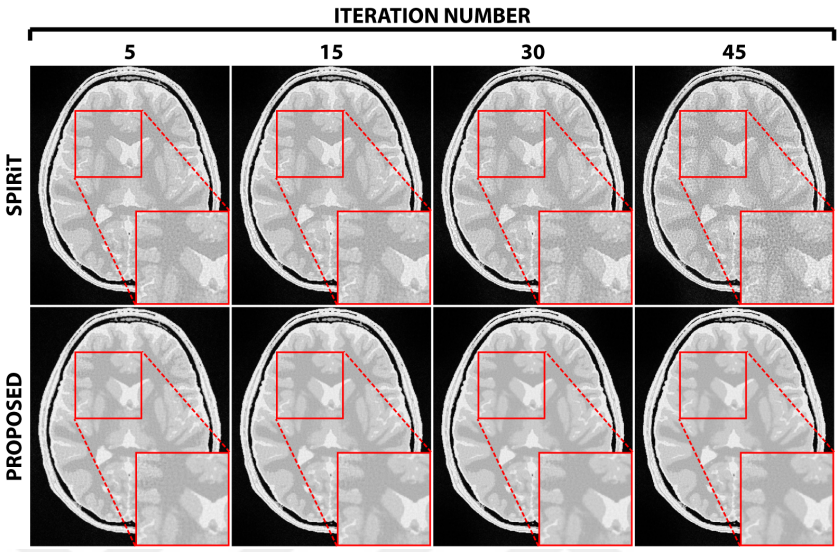

Figure 3.4: Reconstructions of the numerical phantom at distinct iteration numbers for TE = 10 ms. Clearly, the proposed method is more robust against changes in iteration number when compared to SPIRiT. Here, beta was chosen as 0.067 and 0.095 for SPIRiT and the proposed method, respectively (see Fig. 3.2).

that the proposed method yields better results. Quantitative assessment is assessed for three situations: (1) The average PSNR value across the entire map is 29.11 ± 0.22 dB for SPIRiT and 31.12 ± 0.34 dB for SPIRiT$_{\text{hp}}$ (mean $\pm$ SD across contrasts). (2) The average PSNR across the map for optimized Tikhonov parameter is 28.37 ± 0.15 dB for SPIRiT and 30.90 ± 0.28 dB for SPIRiT$_{\text{hp}}$ (3) The average PSNR value for the optimum iteration numbers are 31.84 ± 0.38 dB for SPIRiT and 31.78 ± 0.42 dB for SPIRiT$_{\text{hp}}$. Note that, the conventional ZF reconstructions yield an average PSNR value of 27.96 ± 0.50 dB.

Figure 3.6 shows the representative ZF, SPIRiT and the proposed reconstructions for subject 1 (S1). For representative images, SPIRiT improved PSNR by 3.95 ± 0.21 in S1 and 3.06 ± 0.20 dB in S2 over ZF (mean $\pm$ SD average for across all contrasts). The proposed method improved PSNR by 4.03 ± 0.24 dB in S1 and 3.07 ± 0.30 dB S2 over ZF (mean $\pm$ SD average across all contrasts).

In Figure 3.7, reconstructions at different iterations are demonstrated to show

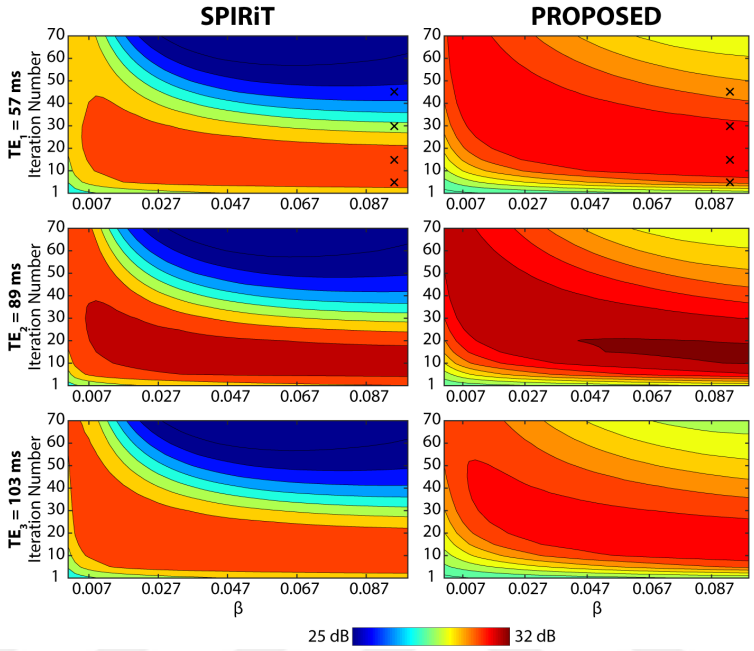

Figure 3.5: *In vivo* comparison of SPIRiT and the proposed method performed for iteration numbers between 1-70 and β between 0.001-0.1. PSNR maps for three different contrasts with TE = 57, 89, and 103 ms are demonstrated. All contrasts for SPIRiT and the proposed method are shown on the same scale for the sake of clarity. PSNR maps show that the proposed method is more robust to parameter selection compared to SPIRiT, especially for iteration number. Black cross signs mark iteration numbers 5, 15, 30, and 45, with reconstructed images shown in Fig. 3.7

the robustness of the proposed method against iteration number. Reconstruction results for iteration 5, 15, 30, and 45 are demonstrated for both subjects. It observed that results are consistent for both S1 and S2. For S1, Tikhonov regularization parameter is selected as 0.093 for SPIRiT and 0.095 the proposed method, respectively. Visual inspection shows that all images from the proposed method are reasonably acceptable whereas SPIRiT results are affected by noise amplification when the iteration number is increased, which confirms the numerical phantom results. Numerical results support this statement (see Table 3.1). SPIRiT improved PSNR by 5.49 ± 2.74 dB in S1 and 6.46 ± 2.49 dB in S2 over ZF (mean $\pm$ SD average across iterations). Whereas proposed method improved PSNR by 8.11 ± 0.50 dB in S1 and 7.32 ± 0.46 dB in S2 over ZF (mean $\pm$ SD average across iterations).

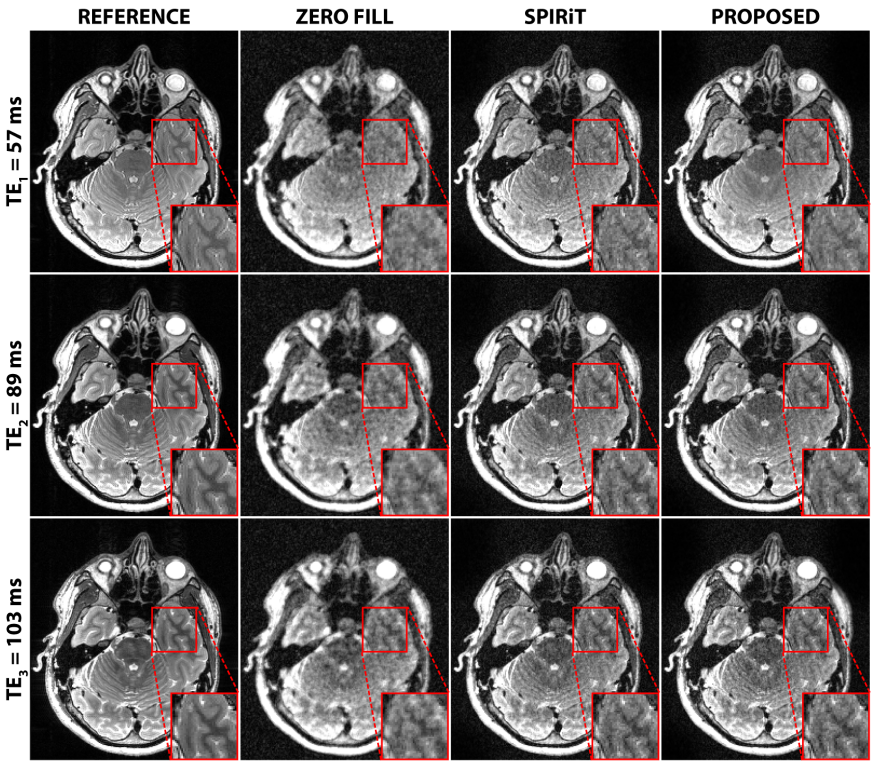

Figure 3.6: Representative reconstructed *in vivo* brain images with TE = 57, 89 and 103 ms. Reconstructions and zoom-in versions of reference, zero fill, SPIRiT, and the proposed methods are demonstrated for R = 3 acceleration. SPIRiT and the proposed method provide improved image quality, with the proposed method having the advantage of robustness against parameter choice.

Table 3.1: PSNR values for different iteration numbers for numerical phantom for TE = 10 ms

ITERATION	**5**	**15**	**30**	**45**
SPIRiT	27.84	28.20	27.07	25.11
PROPOSED	28.46	30.30	31.47	31.96

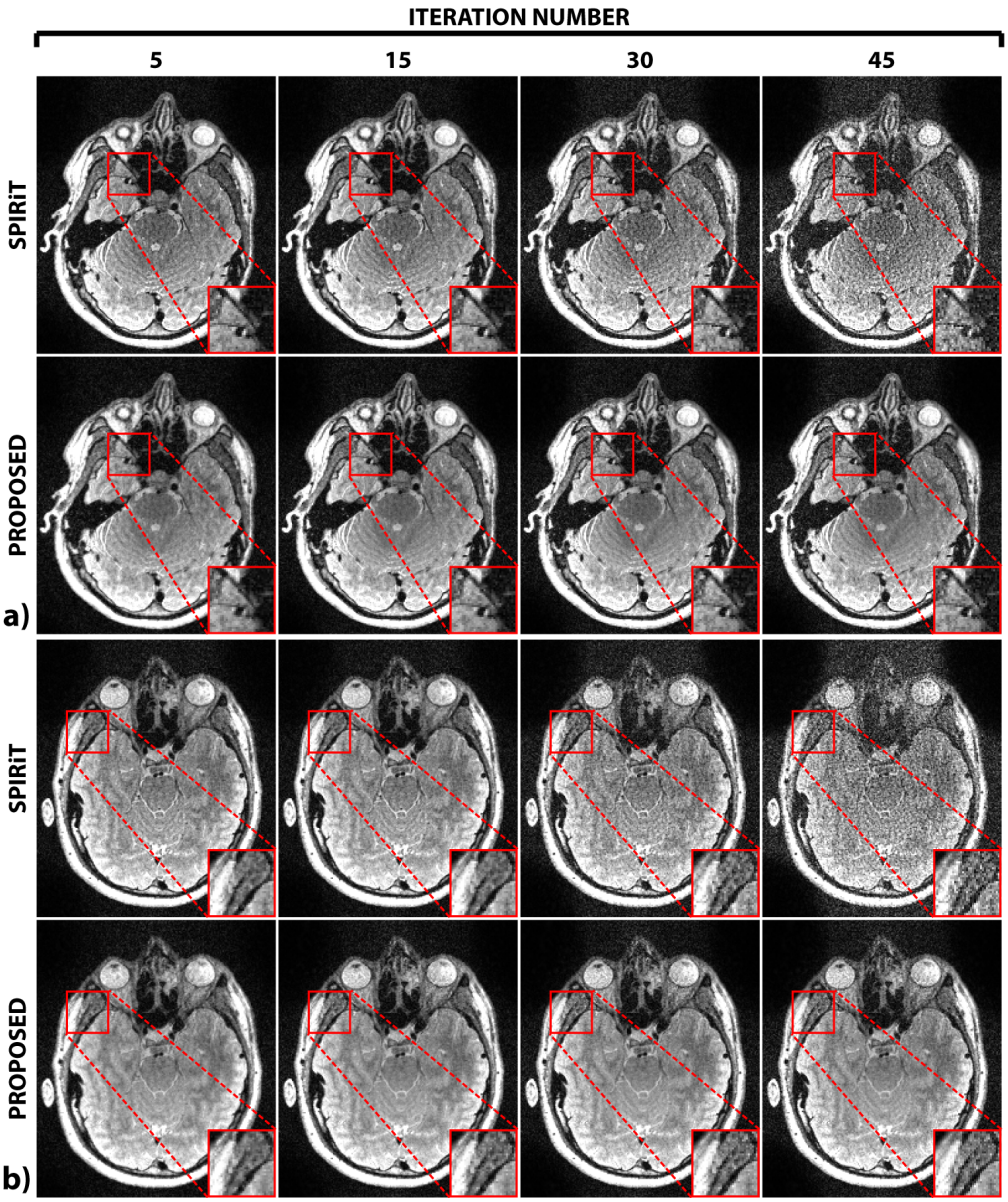

Figure 3.7: Reconstructions of *in vivo* brain images at distinct iteration numbers for TE = 57 ms. a) For subject S1, β was chosen as 0.093 and 0.095 for SPIRiT and the proposed method, respectively. b) For subject S2, beta was chosen as 0.095 for both methods. For both subjects, the scanning parameters and other reconstruction parameters were kept identical.

Table 3.2: PSNR values for different iteration numbers for subject 1 and subject 2 for TE = 103 ms

	ITERATION	**5**	**15**	**30**	**45**
SUBJECT 1	**SPIRiT**	31.59	31.66	29.37	26.38
	PROPOSED	31.19	31.99	31.62	30.83
SUBJECT 2	**SPIRiT**	31.47	31.27	28.68	25.61
	PROPOSED	31.02	31.60	31.25	30.50

3.4 Discussion

This thesis proposes an improved method for reconstructing multiple T_2-weighted acquisitions by filtered kernel estimation. In the SPIRiT$_{hp}$, the estimation of the interpolation kernel is altered for multi-contrast data such that only the intermediate to high spatial frequencies within the calibration region are used. This helps improve kernel estimations by better utilizing correlated information among multiple contrasts. In the reconstruction stage, both interpolation consistency and data fidelity are considered. The filtered kernel estimation in SPIRiT$_{hp}$ yields an improved degree of robustness to selection of reconstruction parameters in both phantom and *in vivo* datasets.

Note that the benefits of SPIRiT$_{hp}$ were more pronounced in simulated phantom results compared to *in vivo* results. This difference could be attributed to the relatively higher spatial resolution inherent to the simulated phantom data compared to *in vivo* data. With the current 3D SPACE sequence, it is challenging to achieve comparable resolutions to the phantom data due to SAR and scan time limitations. These results suggest that the benefits of the proposed technique will be more dominant as the spatial frequency of the acquisitions increases.

In this study, reconstruction results for different iteration numbers and regularization parameters, β, are demonstrated. The other parameters were also evaluated, such as ℓ_2 regularization weight λ, kernel size, scale factor σ, and start and finish points of the high-pass filter. For λ parameter, values that are too small or large reduce reconstruction performance for both SPIRiT and the proposed method. Other than these extreme values, reconstruction is not significantly affected by λ. The scale factor determines the level of emphasis for the low frequencies during kernel estimation. In this thesis, sigma was chosen as zero. Increasing values of sigma affect the proposed method unfavorably, ultimately converging to the performance of SPIRiT for $\sigma = 1$.

Multi-contrast acquisitions in MRI are not limited to multiple T_2-weighted

imaging, but a broad range of contrasts that include T_1, T_2, PD, and diffusion-weighted images [42, 43]. It is expected that the proposed method can be adopted to other multi-contrast applications without major modification. However, in that case, one consideration would be the sequence-related parameters. SNR or robustness to B0 inhomogeneities can change the characteristics of collected data. In that case, the similarity levels of the high frequencies may change from one contrast to another. Thus, the kernel performance may decrease for these scenarios.

This thesis demonstrated the proposed method via retrospective undersampling. For prospective undersampling, the Siemens stock sequence for 3D SPACE was modified to acquire the desired k-space locations only. The details of this modification are given in Appendix A. Demonstrating the proposed method prospectively remains a future work.

In conclusion, improved SPIRiT operator for multiple T_2-weighted images was presented in this thesis. For most of the reconstruction algorithms previously proposed, a specific parameter tuning step is required for the reconstructions to be useful. However, this is a big barrier ahead of the clinical usage of these algorithms. Both simulation and *in vivo* results suggest that the proposed method alleviates this problem as it provides a more flexible parameter selection than conventional SPIRiT.

Chapter 4

Joint Partial Fourier and Compressed Sensing Reconstruction for Accelerated Time-of-Flight Angiography

This chapter is based on the publication titled "Joint Partial Fourier and Compressed Sensing Reconstruction for Accelerated Time-of-Flight MR Angiography", Toygan Kılıç, Tolga Çukur, Oktay Algın and Emine Ülkü Sarıtaş, Proc. of the 26th Signal Processing and Communications Applications Conference, (SIU'18) İzmir, Turkey, 2018.

4.1 Introduction

Time-of-flight (TOF) angiography is a widely used technique, which images intracranial vessels without injecting contrast agents [44]. In this technique, the goal is to increase the contrast between the background (i.e., stationary tissues) and foreground (i.e., the flowing blood). The duration between the RF pulses is

decreased as much as possible to increase this contrast. This way, the stationary tissues are suppressed, whereas the blood flowing inside the vessels is less affected as it is continually renewed. To enhance inflow effects while maintaining high SNR, multi-slab 3D acquisitions are commonly preferred. However, this comes at the cost of prolonged scan times. Previous studies have proposed to use various combinations of parallel imaging (PI) [5], compressed sensing (CS) [7], and partial Fourier (PF) acquisition, all applied along the phase-encode dimensions [45, 46, 47]. Note that when PF acquisition is performed along the phase-encoding dimensions, it interferes with the sampling requirements of PI and, more critically, CS.

Since angiography images are naturally sparse in the spatial domain, CS reconstruction techniques are highly suitable for accelerating their acquisitions [48, 49]. PF acquisition in frequency-encoding direction instead of phase-encoding direction can help increase the SNR due to the resulting shortened TE. In addition, this sampling scheme is compatible with PI and CS techniques. Yet, a direct reconstruction of undersampled k-space data results in excessive blurring in image domain. Therefore, 1D PF reconstruction in the frequency encoding direction is crucial for preserving image resolution. In this thesis, 2D undersampling in phase-encode dimensions and 1D PF data acquisition in frequency-encode dimension is proposed for TOF angiography. Joint reconstruction of these two problems is proposed via a projection-onto-convex-sets (POCS) approach. The proposed method enables time-efficient TOF imaging without necessitating suboptimal sampling patterns, while enabling lower TE to maintain high blood signal.

4.2 Methods

4.2.1 *In Vivo* Experiments

In vivo TOF angiograms in the brain were acquired on a 3T SIEMENS Scanner (MAGNETOM Tim Trio Syngo) using a 32-channel receive-only head coil. R/L

readout dimension (k_x), and S/I (slab direction) (k_z) and A/P phase-encode dimensions (k_y) were used. Other sequence parameters were: 0.44 mm isotropic resolution, TE = 4.24 ms, TR = 21 ms, and 71.35% partial k-space coverage in readout direction, TONE ramp excitation, with a 32-minute total scan time for a fully-sampled acquisition in phase-encode dimensions. A total of 5 slabs were used to cover the entire brain, where each slab contained 48 cross-sections including 50% oversampling. The acquisition matrix for a single slab was of size 274×384×48.

4.2.2 Undersampling Patterns

In this work, prospective and retrospective undersampling patterns were applied to readout and phase-encoding directions, respectively. In phase-encoding directions, a 2D variable Poisson-disc CS undersampling was performed with a 64×32 calibration region. Extra 32 center lines in k_y direction were sampled, because there were less samples in k_z dimension compared to the other two dimensions [50]. The proposed sampling pattern for R = 3.3 is demonstrated in Figure 4.1a. For comparison purposes, PI undersampling was performed using the same calibration region size. For PI undersampling, the number of skipped lines in the phase-encode dimension was adjusted to maintain an identical acceleration rate of R = 3.3. The sampling pattern for PI is demonstrated in Figure 4.1b. For both CS and PI undersampling, %71.35 partial k-space coverage in the readout direction was performed. All compared methods had the same scanning time to ensure a fair comparison of results.

4.2.3 Image Reconstruction

An efficient reconstruction is proposed to recover 3D multi-slab TOF acquisitions undersampled via PF in the readout dimension and CS in the phase-encode dimensions. The proposed reconstruction leverages consecutive CS and PF projections applied iteratively until convergence. The following methods were used

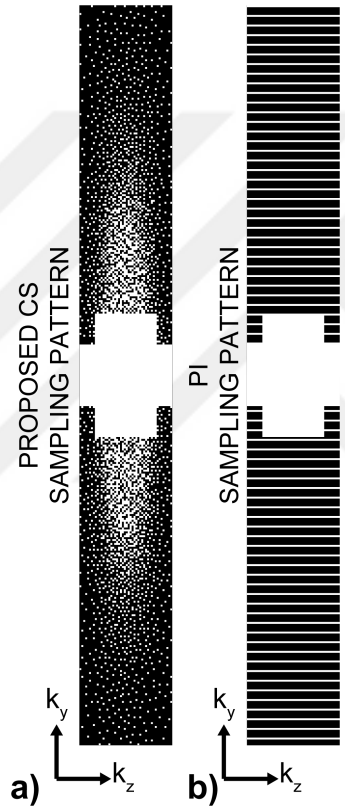

Figure 4.1: Sampling patterns (384×48 matrix). (a) The proposed sampling pattern for compressed sensing (CS) acquisition and (b) parallel imaging sampling pattern (PI). Acceleration was R = 3.3 for both PI and CS. Retrospective undersampling was performed in the two phase-encode dimensions for CS using Poisson-disc sampling with a 64x32 calibration region. In addition to this, 32 extra calibration lines were taken in k_z direction. The same calibration region was maintained for PI, but the number of skipped lines in the phase-encode dimension were adjusted to attain an identical acceleration rate.

for comparison purposes:

- Zero-filled reconstruction (ZF)
- Compressed sensing reconstruction (CS)
- Parallel imaging reconstruction (PI)
- Parallel imaging reconstruction followed by partial Fourier reconstruction (PI+PF)

Reconstruction of data from 32 coils increases the computation time for these methods. Because of this, geometric coil compression was used to map the 32 coils in the original acquisitions to 8 virtual coils for all methods [51]. The images obtained from different coils were combined using sum of squares (SOS) method for all reconstruction methods. For CS reconstruction, SPIRiT was utilized [7]. The details for CS and PF reconstructions are explained in the following sections.

4.2.3.1 Reconstruction using CS

The CS projections were implemented via the conjugate-gradient formulation of 2D SPIRiT (see 2.2.3). For the first iteration, all undersampled locations were zero filled. 1D Fourier transformation was performed along the readout dimension, and each readout section was processed separately. The following optimization problem was solved:

$$\arg\min_{m} \|(Dm - y)\|_2^2 + \lambda \|((G - I)m)\|_2^2 \tag{4.1}$$

Here, m is the reconstructed k-space, y is the acquired data, D is the sampling pattern, G is the interpolation operator, λ is a penalty weight enforcing consistency with the calibration data, here selected as 0.001. A conjugate gradient algorithm was used to solve the above problem. A 9x9 calibration kernel was used for determining the interpolation operator, with a calibration Tikhonov parameter of 0.001. Ten iterations were sufficient for obtaining stable results.

4.2.3.2 Partial Fourier Reconstruction

In this thesis, PF acquisition was applied in the readout direction to increase the contrast between blood and the background. For this purpose, 71.35% of k-space was acquired in the readout direction. The POCS PF algorithm (see 2.2.1) was used to estimate the unacquired part of the k-space. In the implementation of this method, Hann windowing was applied before transformation to image domain, to avoid possible ringing artifacts. Additionally, a 4-pixel wide Fermi window was applied in the transition regions between the acquired and filled parts of the k-space.

4.2.3.3 Proposed Method

The proposed method uses POCS iterations, which utilize successive CS projections and PF projections to increase the resolution and contrast. The following steps were performed for the proposed reconstruction:

1. 1D inverse Fourier transform was applied in the readout direction to separate the 3D problem into 2D problems. Then, each readout section was reconstructed independently.
2. CS reconstruction with SPIRiT interpolator was performed in the phase-encode dimensions, followed by 1D Fourier transform along the readout direction.
3. CS reconstruction also fills the unacquired part of k-space in the readout direction, however, the resulting values are not reliable.
4. PF reconstruction was applied along the readout direction.
5. The resulting k-space was undersampled with the original sampling pattern along the phase-encode directions.Note that, the difference between this k-space and the initial k-space is that the unacquired part along the readout direction has been filled by PF reconstruction.

6. These steps were repeated 3 times. In the last iteration, the output of the PF reconstruction was used as the final image.

The flowchart of the algorithm is given in Figure 4.2.

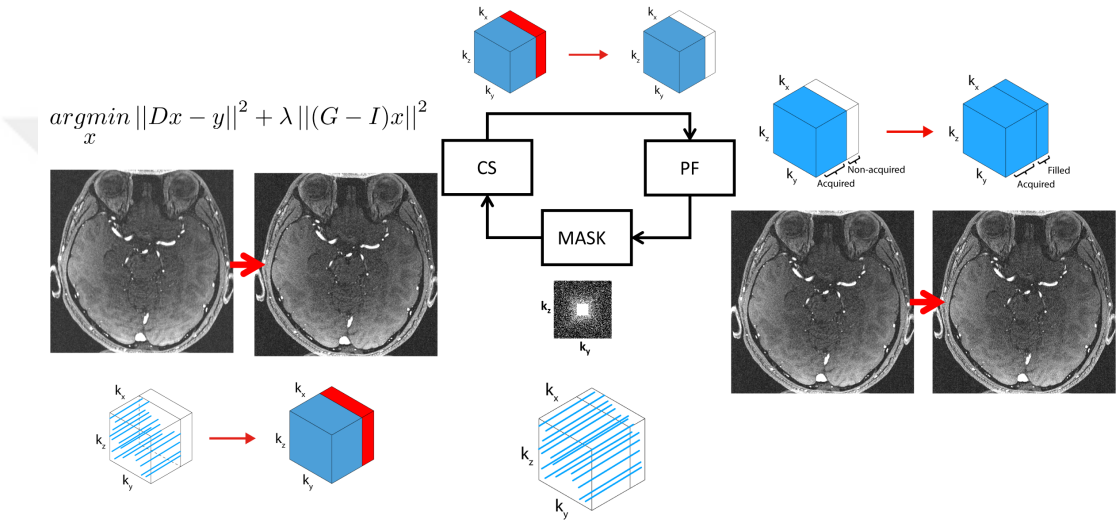

Figure 4.2: Flowchart of the proposed algorithm. Firstly, CS is applied for each readout section. Then, the unreliable values in the unacquired part along the readout direction were replaced with zeros. This empty part was then filled by PF reconstruction. Next, the original undersampling mask was applied along the phase-encode directions. The algorithm iterated 3 times. Then, the output of the PF reconstruction was used as the final image.

4.3 Results

Representative axial cross sections from a 3D TOF acquisition reconstructed by the proposed and comparison methods are displayed in Figure 4.3. Maximum intensity projection (MIP) across a central slab in the brain are shown in Figure 4.4. In these figures, "reference image" refers to the result of PF reconstruction applied on data fully sampled along the phase-encode directions. PI and PI+PF methods suffer from spatial blurring and visible residual aliasing artifacts. CS yields improved artifact suppression, yet it still shows some spatial blurring. In

contrast, the proposed reconstruction achieves high spatial acuity in vessel depiction along with improved artifact suppression. Total processing time for the proposed method was 7 minutes on a workstation with Fujitsu RX300 S8: 2x Intel Xeon E5-2667v2 (16 cores, 3.3 GHz), 128 GB RAM. For PI+PF, PI, and CS the processing times were 3 minutes, 1 minute, and 2 minutes, respectively. Here, the increase in processing time for the proposed method was due to the multiple iterations included. Faster reconstructions can be obtained using GPUs, if needed.

Peak Signal-to-Noise Ratio (PSNR) metric was used to quantitatively assess the performance of the proposed and compared methods. For calculation of PSNR metric, first the square of the peak pixel value in reference image was divided by the mean-square error between reference and reconstructed images. Then, the final result for PSNR was calculated in decibel (dB) unit. MATLAB *psnr* built-in function was used for this purpose. PSNR results for MIP are as follows: 31.36 dB for ZF reconstruction, 28.61 dB for PI, 31.90 dB for CS, 28.14 dB for PI+PF, and 32.48 dB for proposed reconstruction. These results show that the improvement in MIP seen via visual inspection is confirmed by quantitative assessment via PSNR.

The results in this thesis were demonstrated via retrospective undersampling. To acquire only the desired k-space locations prospectively, the Siemens stock sequence for TOF was modified, as given in Appendix B. *In vivo* demonstrations of the proposed method with prospective undersampling remains a future work.

4.4 Conclusion

Here, we considered TOF acquisitions comprising 2D acceleration in the phase-encode directions to increase scan efficiency, along with PF in the readout-direction to minimize signal losses. Previous work used both PF and CS in phase-encode dimensions, with conflicting requirements. The main goal of the proposed technique is to use PF in readout direction to increase the contrast

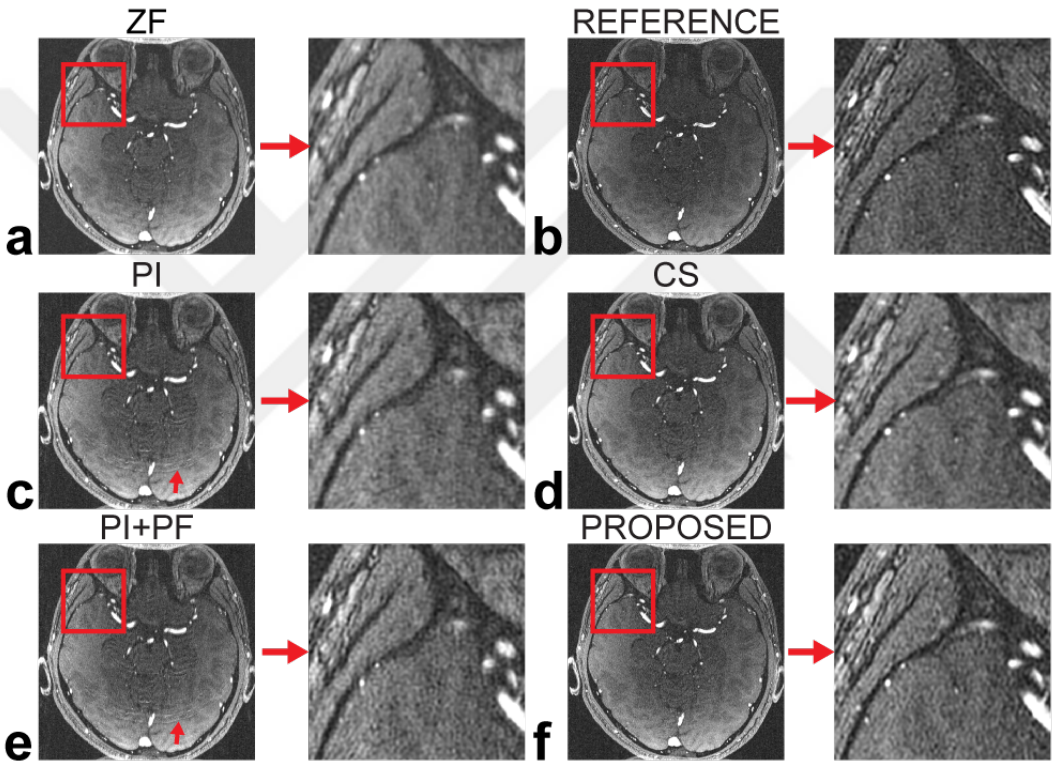

Figure 4.3: Reconstruction results for the proposed and comparison methods for a representative axial slice. (a) Zero-filled reconstruction, (b) reference image, (c) standard PI reconstruction, (d) standard CS reconstruction (e) standard PI followed by PF, and (f) the proposed method. PI and PI+PF methods suffer from spatial blurring and visible residual aliasing artifacts. CS yields improved artifact suppression, yet it still shows some spatial blurring. In contrast, the proposed reconstruction shows high spatial acuity in vessel depiction along with improved artifact suppression.

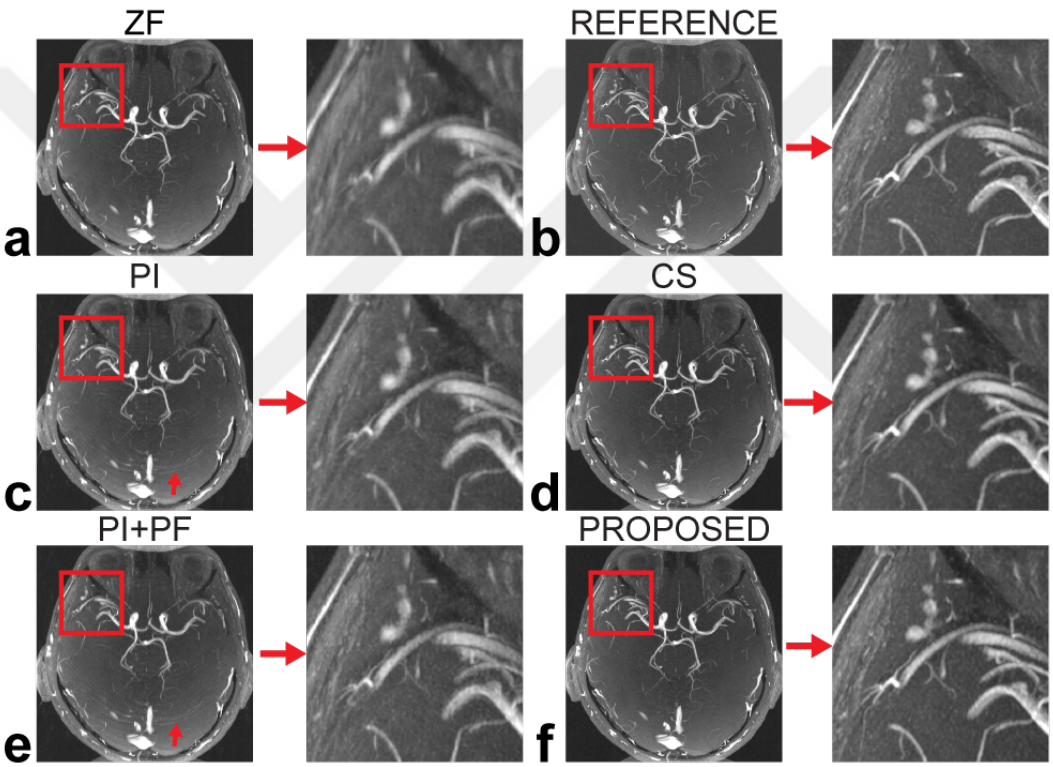

Figure 4.4: Reconstruction results for MIP across a central slab in the brain (a) Zero-filled reconstruction, (b) reference image, (c) standard PI reconstruction, (d) standard CS reconstruction (e) standard PI followed by PF, and (f) the proposed method.(d) Although CS usage decreases the aliasing artifacts, it does not sufficiently improve image resolution when used alone. (f) On the other hand, the proposed method increases the resolution and enhances the visibility of the vessels.

between the background and blood signal. We proposed a reconstruction framework that iteratively alternates between CS projections in the 2D phase-encode direction and PF projections along the readout. When compared to alternative techniques, the proposed framework yields high-spatial-resolution angiograms in the brain with improved suppression of aliasing artifacts.

Chapter 5

Conclusion

In this thesis, two different methods have been proposed for multiple T_2-weighted and TOF angiography MRI images to reduce the scanning time and increase the image quality.

First, the kernel estimation of multiple T_2-weighted images with acquired different TE values is improved for SPIRiT method. The conventional and proposed method were comparatively evaluated for different reconstruction parameter values for both the simulated brain phantom and *in vivo* datasets. The results have shown that the proposed method increases the robustness of the interpolator against Tikhonov regularization parameter and the iteration number. Although the improved kernel estimation for multiple T_2-weighted images provides a crucial improvement to automate parameter selection, fully automated solutions should be considered for clinical use. Investigation of automatic parameter selection for the proposed method remains as future work.

Second, a new framework for TOF angiography image reconstruction was introduced. Previously, combinations of PI, CS and PF techniques utilized phase-encode dimensions are introduced to reduce scanning time. The proposed method decreases the scanning time via undersampling the phase-encode directions and

increases the signal level in blood vessels by partial acquisition in readout direction. PSNR results of the proposed method for *in vivo* TOF angiography images show that the PF reconstruction in readout direction helps to increase resolution. Yet, in the current study partial acquisition was 71.35% in readout direction. A future prospective study that acquires fewer data in readout direction may benefit from reduced TE so that increased signal level for blood vessels.

Bibliography

[1] P. C. Lauterbur *et al.*, "Image formation by induced local interactions: examples employing nuclear magnetic resonance," 1973.

[2] J. Hennig, A. Nauerth, and H. Friedburg, "Rare imaging: a fast imaging method for clinical mr," *Magnetic resonance in medicine*, vol. 3, no. 6, pp. 823–833, 1986.

[3] F. W. Wehrli, "Time-of-flight effects in mr imaging of flow," *Magnetic resonance in medicine*, vol. 14, no. 2, pp. 187–193, 1990.

[4] J. P. Mugler III, "Optimized three-dimensional fast-spin-echo mri," *Journal of Magnetic Resonance Imaging*, vol. 39, no. 4, pp. 745–767, 2014.

[5] M. A. Griswold, P. M. Jakob, R. M. Heidemann, M. Nittka, V. Jellus, J. Wang, B. Kiefer, and A. Haase, "Generalized autocalibrating partially parallel acquisitions (grappa)," *Magnetic resonance in medicine*, vol. 47, no. 6, pp. 1202–1210, 2002.

[6] K. P. Pruessmann, M. Weiger, M. B. Scheidegger, P. Boesiger, *et al.*, "Sense: sensitivity encoding for fast mri," *Magnetic resonance in medicine*, vol. 42, no. 5, pp. 952–962, 1999.

[7] M. Lustig and J. M. Pauly, "SPIRiT: Iterative self-consistent parallel imaging reconstruction from arbitrary k-space," *Magnetic Resonance in Medicine*, vol. 64, no. 2, pp. 457–471, 2010.

[8] B. Bilgic, V. K. Goyal, and E. Adalsteinsson, "Multi-contrast reconstruction with Bayesian compressed sensing," *Magnetic Resonance in Medicine*, vol. 66, no. 6, pp. 1601–1615, 2011.

[9] J. Huang, C. Chen, and L. Axel, "Fast multi-contrast MRI reconstruction," *Magnetic Resonance Imaging*, vol. 32, no. 10, pp. 1344–1352, 2014.

[10] A. Majumdar and R. K. Ward, "Joint reconstruction of multiecho MR images using correlated sparsity," *Magnetic Resonance Imaging*, vol. 29, no. 7, pp. 899–906, 2011.

[11] M. Lustig, D. Donoho, and J. M. Pauly, "Sparse MRI: The application of compressed sensing for rapid MR imaging," *Magnetic Resonance in Medicine*, vol. 58, no. 6, pp. 1182–1195, 2007.

[12] E. Haacke, E. Lindskogj, and W. Lin, "A fast, iterative, partial-fourier technique capable of local phase recovery," *Journal of Magnetic Resonance (1969)*, vol. 92, no. 1, pp. 126–145, 1991.

[13] J. Larmor, "Lxiii. on the theory of the magnetic influence on spectra; and on the radiation from moving ions," *The London, Edinburgh, and Dublin Philosophical Magazine and Journal of Science*, vol. 44, no. 271, pp. 503–512, 1897.

[14] E. U. Saritas, C. H. Cunningham, J. H. Lee, E. T. Han, and D. G. Nishimura, "Dwi of the spinal cord with reduced fov single-shot epi," *Magnetic Resonance in Medicine: An Official Journal of the International Society for Magnetic Resonance in Medicine*, vol. 60, no. 2, pp. 468–473, 2008.

[15] E. U. Saritas, D. Lee, T. Cukur, A. Shankaranarayanan, and D. G. Nishimura, "Hadamard slice encoding for reduced-fov diffusion-weighted imaging," *Magnetic resonance in Medicine*, vol. 72, no. 5, pp. 1277–1290, 2014.

[16] M. Uecker, P. Lai, M. J. Murphy, P. Virtue, M. Elad, J. M. Pauly, S. S. Vasanawala, and M. Lustig, "Espirit—an eigenvalue approach to autocalibrating parallel mri: where sense meets grappa," *Magnetic resonance in medicine*, vol. 71, no. 3, pp. 990–1001, 2014.

[17] P. Kellman and E. R. McVeigh, "Image reconstruction in snr units: a general method for snr measurement," *Magnetic resonance in medicine*, vol. 54, no. 6, pp. 1439–1447, 2005.

[18] E. L. Hahn, "Spin echoes," *Physical review*, vol. 80, no. 4, p. 580, 1950.

[19] J. Hennig, M. Weigel, and K. Scheffler, "Multiecho sequences with variable refocusing flip angles: optimization of signal behavior using smooth transitions between pseudo steady states (traps)," *Magnetic Resonance in Medicine: An Official Journal of the International Society for Magnetic Resonance in Medicine*, vol. 49, no. 3, pp. 527–535, 2003.

[20] D. C. Alsop, "The sensitivity of low flip angle rare imaging," *Magnetic resonance in medicine*, vol. 37, no. 2, pp. 176–184, 1997.

[21] I.-C. Kiricuta and V. Simplăceanu, "Tissue water content and nuclear magnetic resonance in normal and tumor tissues," *Cancer research*, vol. 35, no. 5, pp. 1164–1167, 1975.

[22] R. S. Briellmann, A. Syngeniotis, S. Fleming, R. M. Kalnins, D. F. Abbott, and G. D. Jackson, "Increased anterior temporal lobe T2 times in cases of hippocampal sclerosis: a multi-echo T2 relaxometry study at 3T," *American Journal of Neuroradiology*, vol. 25, no. 3, pp. 389–394, 2004.

[23] H.-L. Margaret Cheng, N. Stikov, N. R. Ghugre, and G. A. Wright, "Practical medical applications of quantitative mr relaxometry," *Journal of Magnetic Resonance Imaging*, vol. 36, no. 4, pp. 805–824, 2012.

[24] H. M. Pappius, "Fundamental aspects of brain edema," *Handbook of clinical neurology*, vol. 16, no. Part 1, pp. 167–185, 1974.

[25] P. Tofts, *Quantitative MRI of the brain: measuring changes caused by disease*. John Wiley & Sons, 2005.

[26] E. Gong, F. Huang, K. Ying, W. Wu, S. Wang, and C. Yuan, "PROMISE: Parallel-imaging and compressed-sensing reconstruction of multicontrast imaging using SharablE information," *Magnetic Resonance in Medicine*, vol. 73, no. 2, pp. 523–535, 2015.

[27] E. Biyik, E. Ilicak, and T. Çukur, "Reconstruction by calibration over tensors for multi-coil multi-acquisition balanced ssfp imaging," *Magnetic resonance in medicine*, vol. 79, no. 5, pp. 2542–2554, 2018.

[28] E. Ilicak, L. K. Senel, E. Biyik, and T. Çukur, "Profile-encoding reconstruction for multiple-acquisition balanced steady-state free precession imaging," *Magnetic resonance in medicine*, vol. 78, no. 4, pp. 1316–1329, 2017.

[29] T. Zhang, J. M. Pauly, and I. R. Levesque, "Accelerating parameter mapping with a locally low rank constraint," *Magnetic resonance in medicine*, vol. 73, no. 2, pp. 655–661, 2015.

[30] D. Lee, K. H. Jin, E. Y. Kim, S.-H. Park, and J. C. Ye, "Acceleration of mr parameter mapping using annihilating filter-based low rank hankel matrix (aloha)," *Magnetic resonance in medicine*, vol. 76, no. 6, pp. 1848–1864, 2016.

[31] L. K. Senel, T. Kilic, A. Gungor, E. Kopanoglu, H. E. Guven, E. U. Saritas, A. Koc, and T. Cukur, "Statistically Segregated k-Space Sampling for Accelerating Multiple-Acquisition MRI," *arXiv preprint arXiv:1710.00532*, 2017.

[32] E. Biyik, E. Ilicak, and T. Çukur, "Reconstruction by calibration over tensors for multi-coil multi-acquisition balanced SSFP imaging," *Magnetic Resonance in Medicine*, 2017.

[33] B. Bilgic, T. H. Kim, C. Liao, M. K. Manhard, L. L. Wald, J. P. Haldar, and K. Setsompop, "Improving parallel imaging by jointly reconstructing multi-contrast data," *Magnetic Resonance in Medicine*, 2018.

[34] A. Majumdar and R. K. Ward, "Accelerating multi-echo T2 weighted MR imaging: analysis prior group-sparse optimization," *Journal of Magnetic Resonance*, vol. 210, no. 1, pp. 90–97, 2011.

[35] A. Majumdar and R. Ward, "Rank awareness in group-sparse recovery of multi-echo MR images," *Sensors*, vol. 13, no. 3, pp. 3902–3921, 2013.

[36] M. Murphy, M. Alley, J. Demmel, K. Keutzer, S. Vasanawala, and M. Lustig, "Fast ℓ_1-SPIRiT Compressed Sensing Parallel Imaging MRI: Scalable Parallel Implementation and Clinically Feasible Runtime," *IEEE Transactions on Medical Imaging*, vol. 31, no. 6, pp. 1250–1262, 2012.

[37] C. C. Paige and M. A. Saunders, "LSQR: An algorithm for sparse linear equations and sparse least squares," *ACM transactions on mathematical software*, vol. 8, no. 1, pp. 43–71, 1982.

[38] B. Aubert-Broche, A. C. Evans, and L. Collins, "A new improved version of the realistic digital brain phantom," *NeuroImage*, vol. 32, no. 1, pp. 138–145, 2006.

[39] J. I. Tamir, M. Uecker, W. Chen, P. Lai, M. T. Alley, S. S. Vasanawala, and M. Lustig, "T2 shuffling: Sharp, multicontrast, volumetric fast spin-echo imaging," *Magnetic Resonance in Medicine*, vol. 77, no. 1, pp. 180–195, 2017.

[40] S. M. Smith, M. Jenkinson, M. W. Woolrich, C. F. Beckmann, T. E. Behrens, H. Johansen-Berg, P. R. Bannister, M. De Luca, I. Drobnjak, D. E. Flitney, *et al.*, "Advances in functional and structural MR image analysis and implementation as FSL," *Neuroimage*, vol. 23, pp. S208–S219, 2004.

[41] D. O. Walsh, A. F. Gmitro, and M. W. Marcellin, "Adaptive reconstruction of phased array MR imagery," *Magnetic Resonance in Medicine*, vol. 43, no. 5, pp. 682–690, 2000.

[42] W. Liu, X. Zhao, Y. Ma, X. Tang, and J.-H. Gao, "Dwi using navigated interleaved multishot epi with realigned grappa reconstruction," *Magnetic resonance in medicine*, vol. 75, no. 1, pp. 280–286, 2016.

[43] X. Ma, Z. Zhang, E. Dai, and H. Guo, "Improved multi-shot diffusion imaging using grappa with a compact kernel," *Neuroimage*, vol. 138, pp. 88–99, 2016.

[44] D. G. Nishimura, "Time-of-flight mr angiography," *Magnetic resonance in medicine*, vol. 14, no. 2, pp. 194–201, 1990.

[45] M. Doneva, P. Börnert, H. Eggers, and A. Mertins, "Partial fourier compressed sensing," in *Proc. Intl. Soc. Mag. Reson. Med*, vol. 18, p. 4851, 2010.

[46] T. Küstner, C. Würslin, S. Gatidis, P. Martirosian, K. Nikolaou, N. Schwenzer, F. Schick, B. Yang, and H. Schmidt, "Mr image reconstruction using a combination of compressed sensing and partial fourier acquisition: Espresso," *IEEE transactions on medical imaging*, vol. 35, no. 11, pp. 2447–2458, 2016.

[47] G. Li, J. Hennig, E. Raithel, M. Büchert, D. Paul, J. G. Korvink, and M. Zaitsev, "An l1-norm phase constraint for half-fourier compressed sensing in 3d mr imaging," *Magnetic Resonance Materials in Physics, Biology and Medicine*, vol. 28, no. 5, pp. 459–472, 2015.

[48] T. Çukur, M. Lustig, and D. G. Nishimura, "Improving non-contrast-enhanced steady-state free precession angiography with compressed sensing," *Magnetic Resonance in Medicine: An Official Journal of the International Society for Magnetic Resonance in Medicine*, vol. 61, no. 5, pp. 1122–1131, 2009.

[49] T. Cukur, M. Lustig, E. U. Saritas, and D. G. Nishimura, "Signal compensation and compressed sensing for magnetization-prepared mr angiography," *IEEE transactions on medical imaging*, vol. 30, no. 5, p. 1017, 2011.

[50] Y. Fushimi, T. Okada, T. Kikuchi, A. Yamamoto, T. Okada, T. Yamamoto, M. Schmidt, K. Yoshida, S. Miyamoto, and K. Togashi, "Clinical evaluation of time-of-flight mr angiography with sparse undersampling and iterative reconstruction for cerebral aneurysms," *NMR in Biomedicine*, vol. 30, no. 11, p. e3774, 2017.

[51] T. Zhang, J. M. Pauly, S. S. Vasanawala, and M. Lustig, "Coil compression for accelerated imaging with cartesian sampling," *Magnetic resonance in medicine*, vol. 69, no. 2, pp. 571–582, 2013.

Appendix A

3D SPACE Sequence Modification for Prospective Undersampling

In Chapter 3, reconstruction results from retrospective undersampling cases were shown for joint multi-contrast reconstruction of T_2-weighted images. For prospective undersampling purposes, the Siemens stock sequence for 3D SPACE was modified such that only the desired k-space points could be acquired. In this section, timing diagrams for the modified 3D SPACE sequence are demonstrated. In addition, phantom and in vivo validations of the prospective sampling scheme are provided.

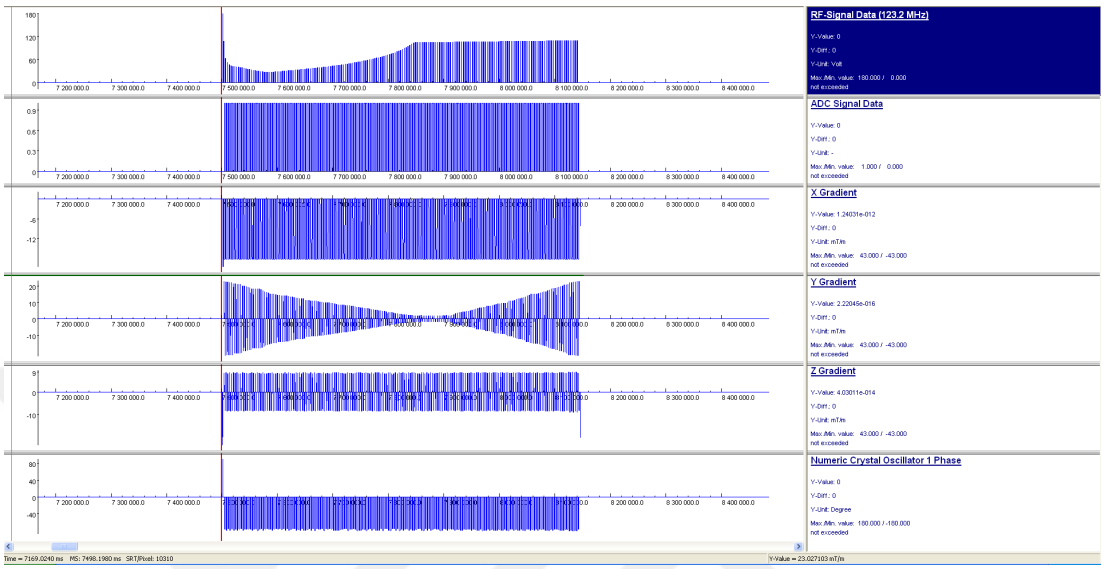

Figure A.1: Sequence diagram of SPACE for one repetition time. For the case of fully sampled k-space, consecutive phase-encoding gradient amplitudes would vary linearly with time. Due to random undersampling of k-space, consecutive gradient amplitudes in y and z directions vary in a nonlinear but still monotonic fashion in the modified SPACE sequence.

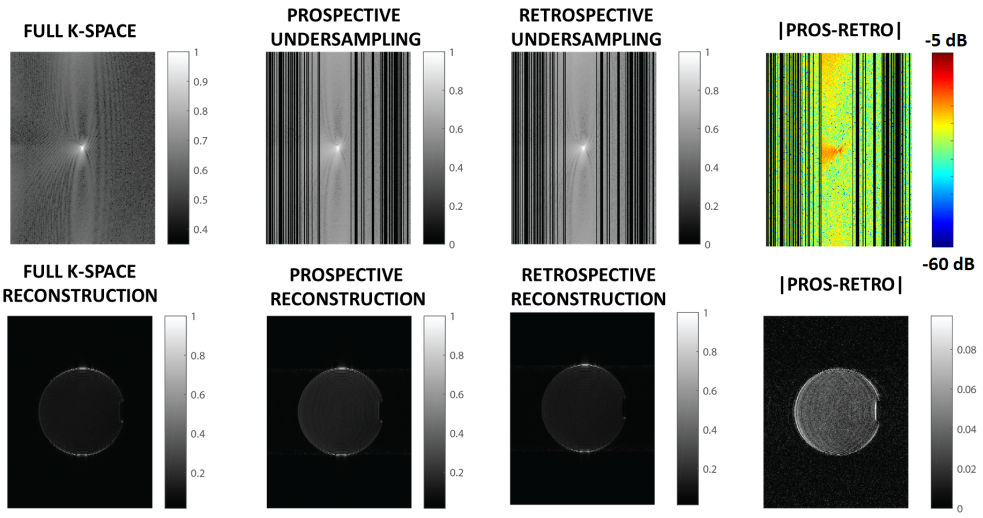

Figure A.2: Validation of the prospective undersampling scheme on a doped water phantom in axial plane. The first row shows from left to right the full k-space acquisition, prospectively undersampled k-space, retrospectively undersampled k-space, and the difference between prospective and retrospective undersampling in units of dB. The second row shows the corresponding image domain results. An acceleration factor of R = 2 was used for this validation experiment.

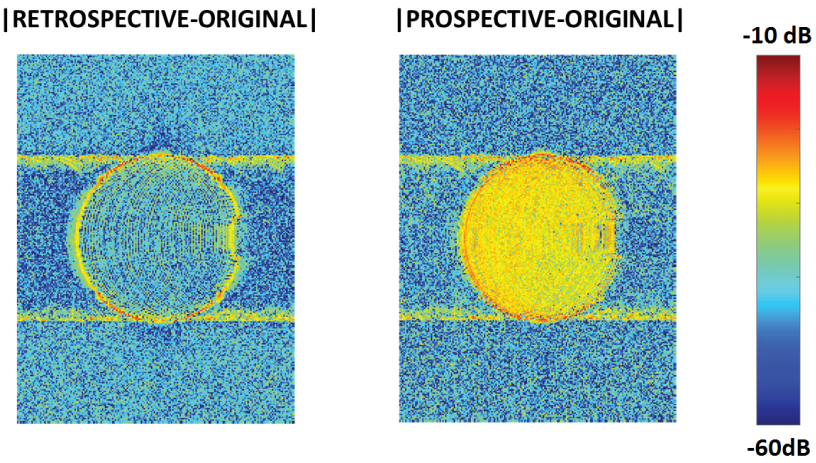

Figure A.3: Difference images for the doped water phantom. [Left] The absolute difference between the original (i.e., full k-space) image and retrospectively undersampled zero-fill image, and [Right] the absolute difference between the original image and prospectively undersampled zero-fill image, in units of dB. An acceleration factor of R = 6 was used in this validation experiment.

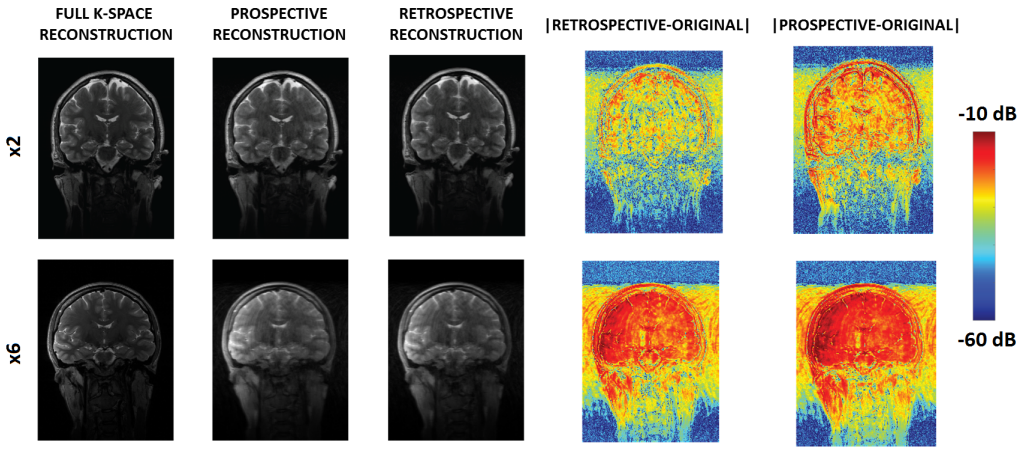

Figure A.4: Validation of the prospective undersampling scheme for *in vivo* brain imaging. The first row shows from left to right the full k-space reconstruction, prospectively undersampled reconstruction, retrospectively undersampled reconstruction, the absolute difference between retrospective undersampling and full k-space reconstructions, and the absolute difference between prospective reconstruction and full k-space reconstruction in units of dB. An acceleration factor of R = 2 was used in the top row, and R = 6 was used in the bottom row.

Appendix B

TOF Sequence Modification for Prospective Undersampling

In Chapter 4, reconstruction results from retrospective undersampling cases were shown for joint PF and CS reconstruction for accelerated TOF. For prospective undersampling purposes, the Siemens stock sequence for TOF was modified such that only the desired k-space points could be acquired. In this section, timing diagrams for the modified TOF sequence are demonstrated. In addition, phantom and *in vivo* validations of the prospective sampling scheme are provided.

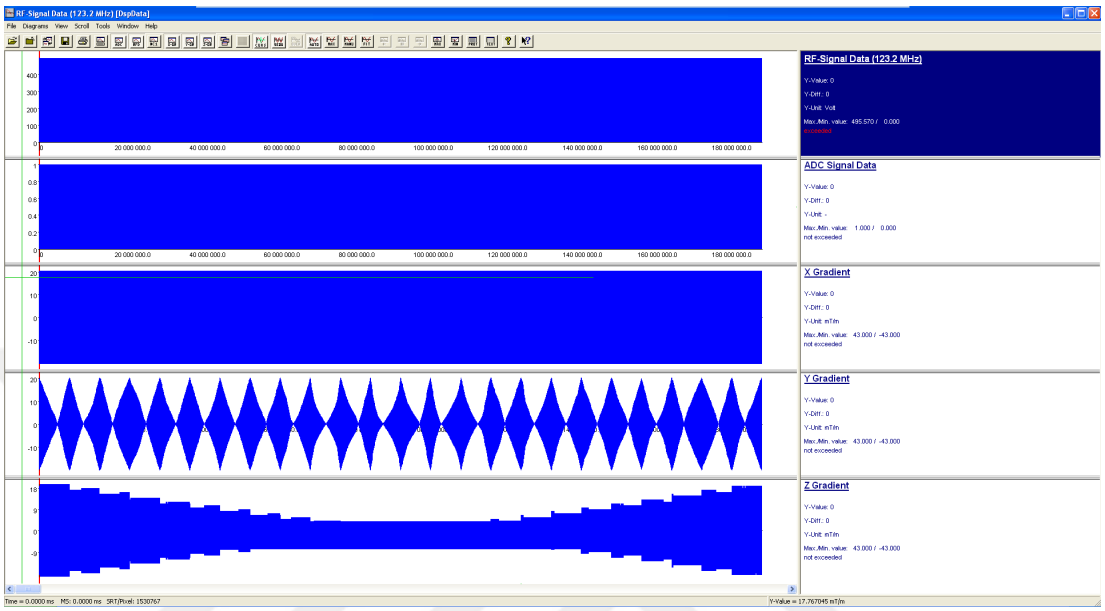

Figure B.1: The general timing diagram of the undersampled TOF sequence. The timing diagrams of y and z gradients show that the z-axis is used as the outer loop and the y-axis is used as the inner loop. The details for one TR of TOF sequence is shown in Fig.B.2.

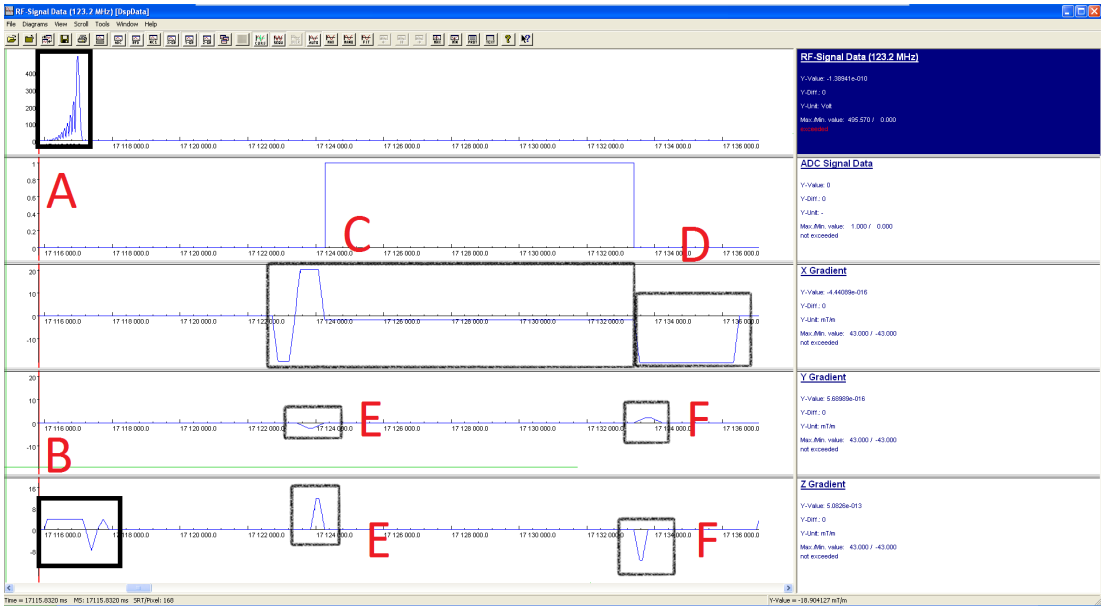

Figure B.2: One TR of the TOF sequence. A: asymmetric RF excitation, B: slice selective gradient, C: readout gradient, D: spoiler gradient, E: phase encoding gradients, and F: rewinder gradients.

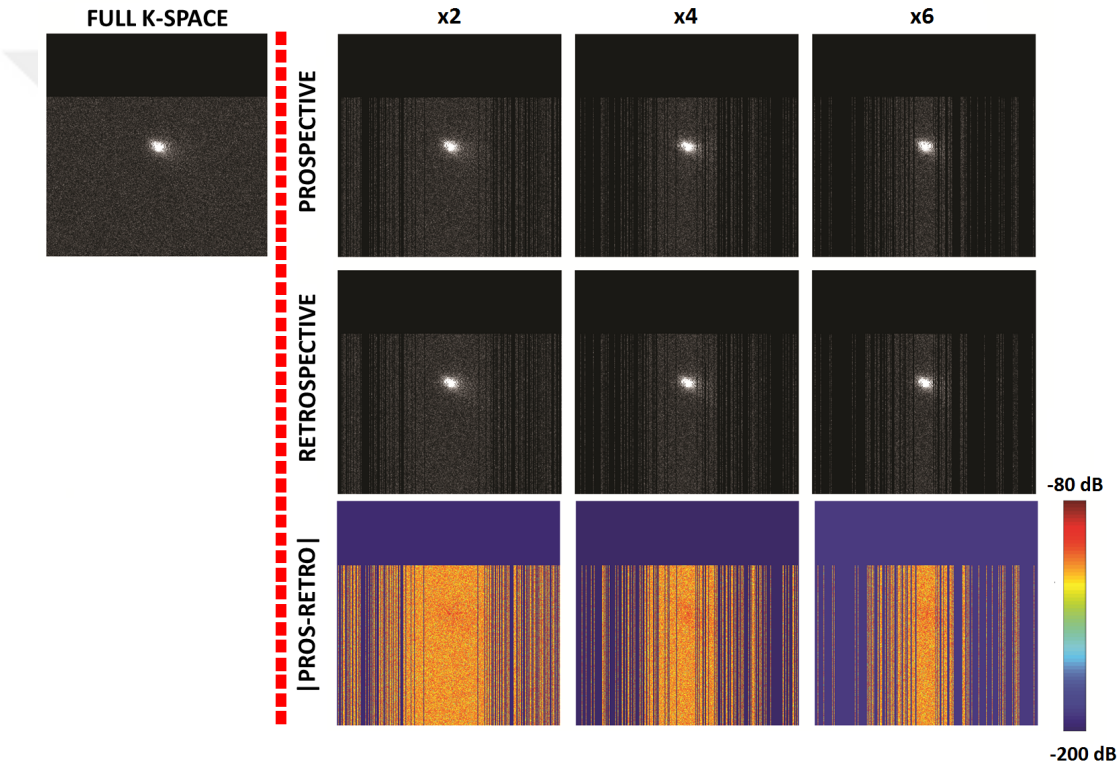

Figure B.3: Validation of the prospective undersampling scheme on a doped water phantom in axial plane, for acceleration factors of R = 2, 4, and 6. Since the PF acquisition was applied in the readout direction, 274 samples were collected instead of the full 384 samples. The figure shows full k-space (with PF acquision), prospectively undersampled k-space, retrospectively undersampled k-space, and the error maps.

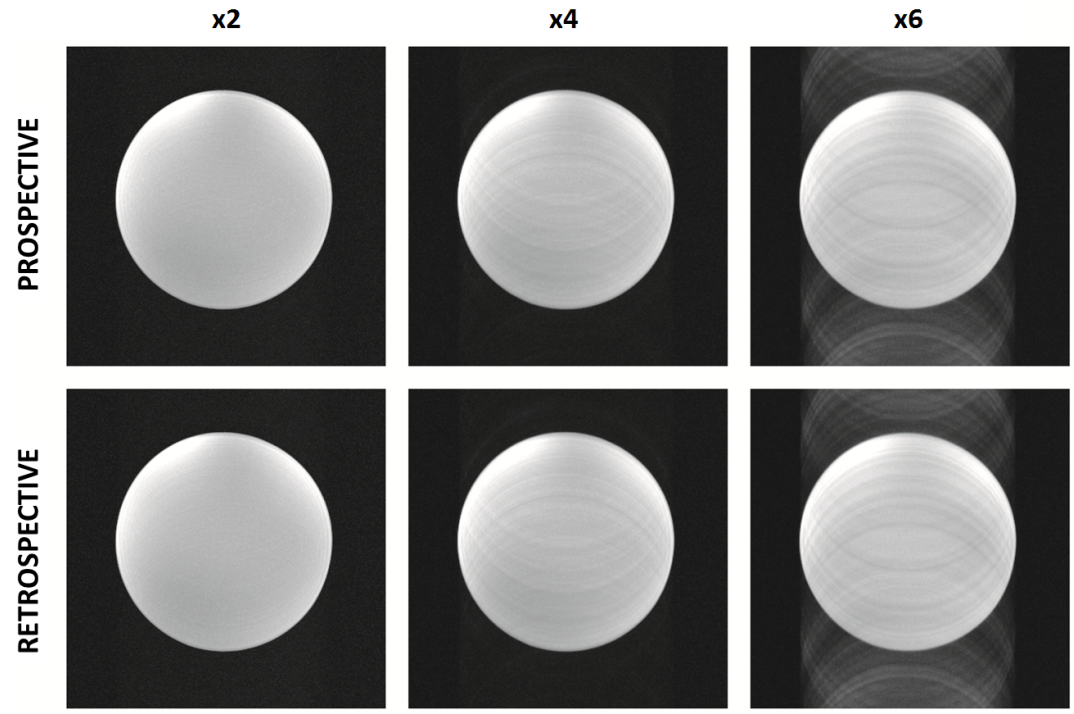

Figure B.4: Zero-fill reconstruction results for prospective and restrospective undersampling on the doped water phantom, for acceleration factors of R = 2, 4, and 6.

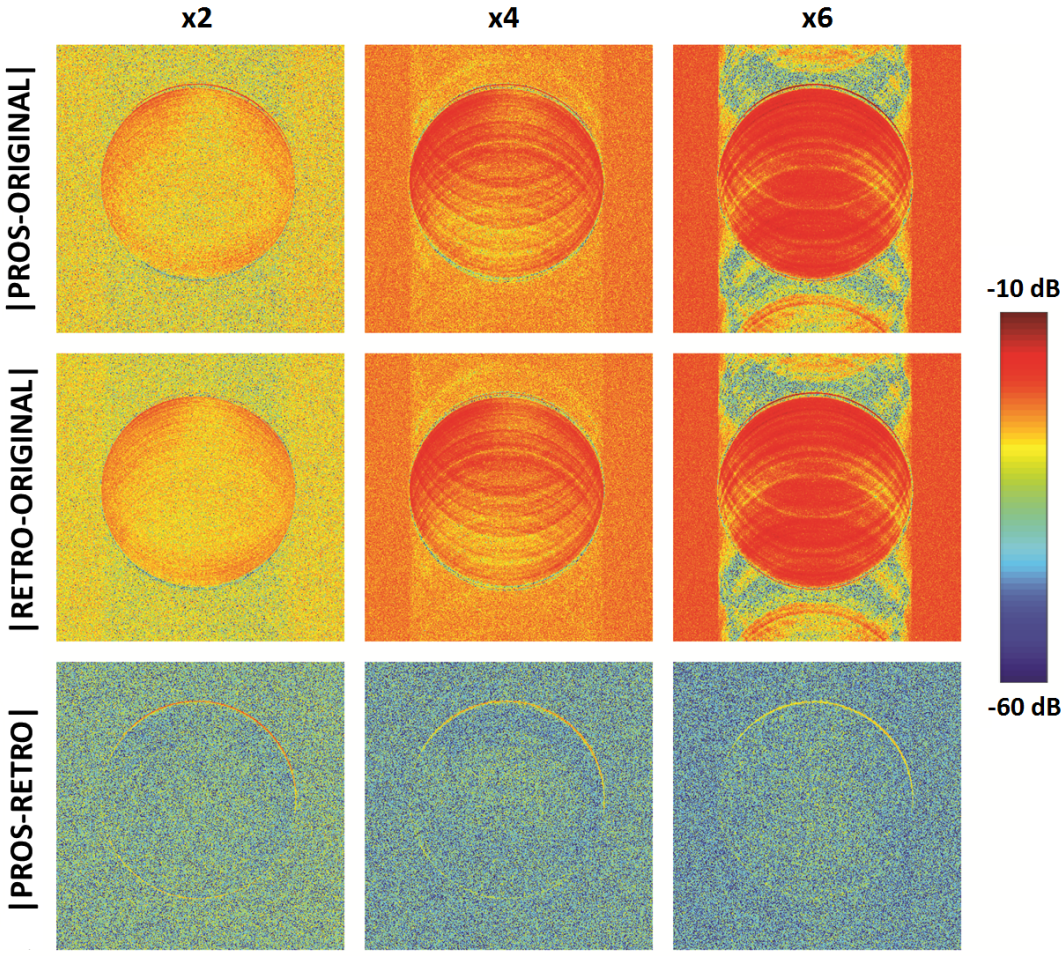

Figure B.5: The difference maps among zero-filled reconstructions of prospective and retrospective undersampling, and fully sampled reconstruction obtained from the phantom experiments are shown in units of dB, for acceleration factors of R = 2, 4, and 6. The first and the second rows show the difference maps with respect to fully sampled k-space reconstruction. The last row shows the difference between the zero-filled reconstructions of prospective and retrospective undersampling. As expected, the error increases for both prospective and retrospective undersampling as the acceleration factor increases.

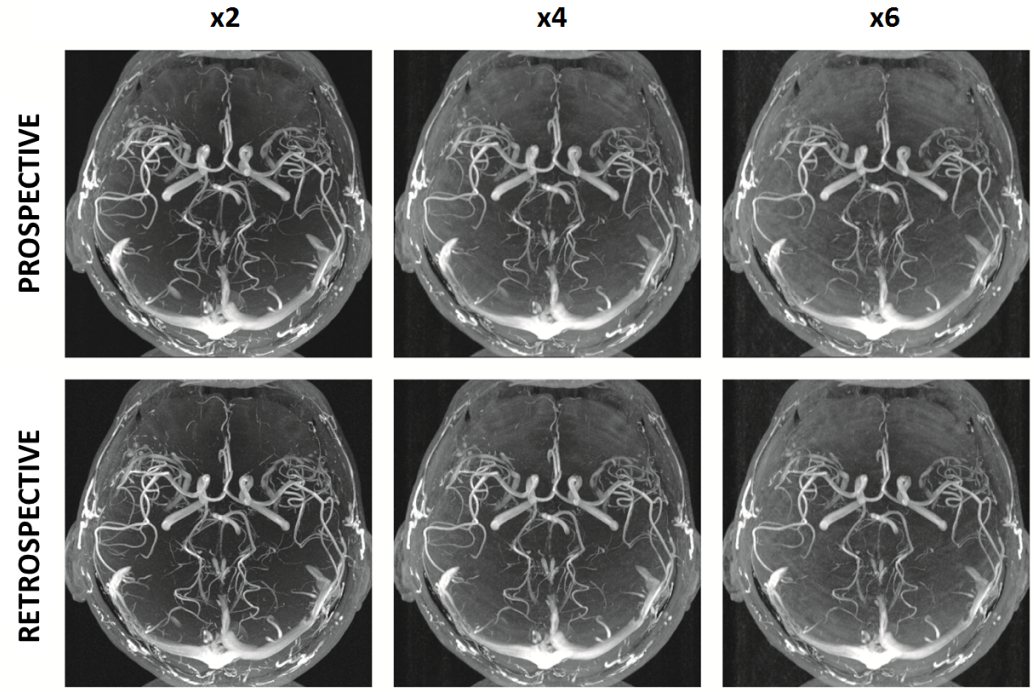

Figure B.6: Validation of the prospective undersampling scheme for *in vivo* brain imaging. MIP images from zero-filled reconstructions of prospective and retrospective undersampling are shown for acceleration factors of R = 2, 4, and 6.

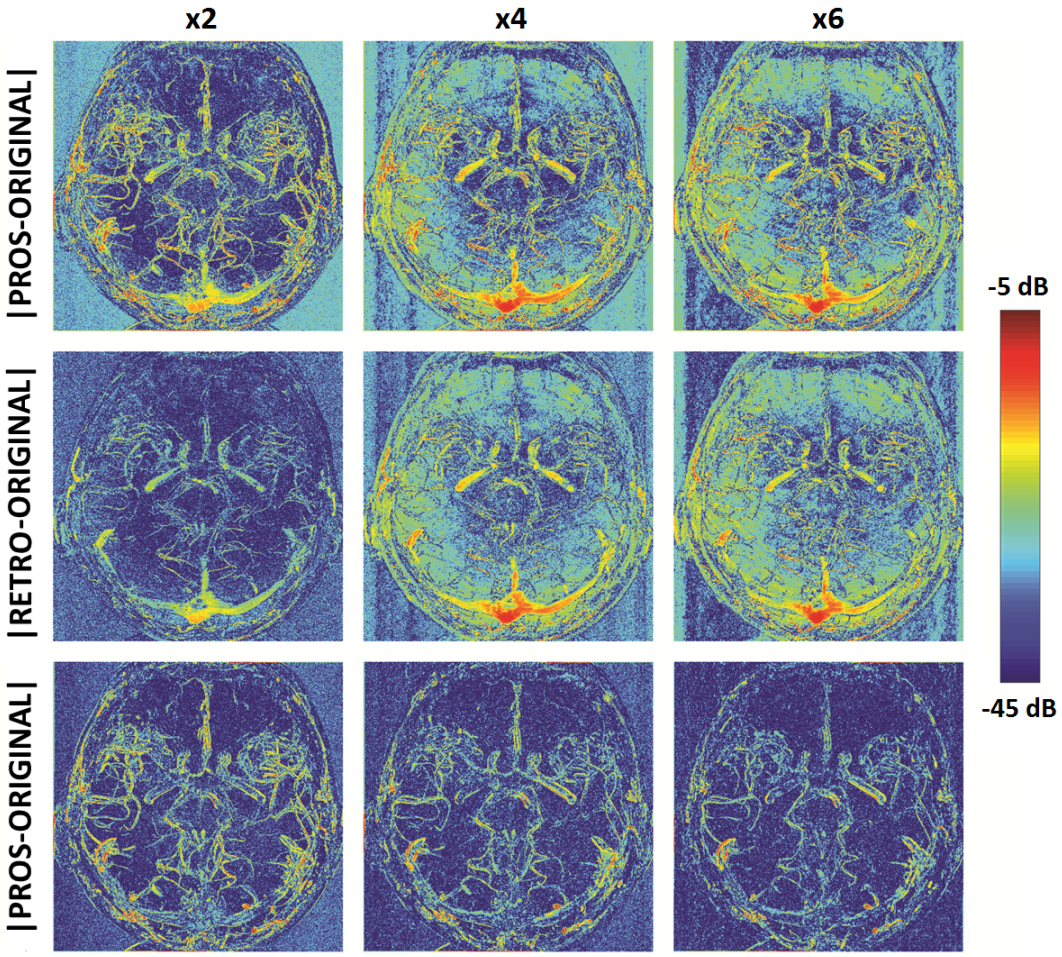

Figure B.7: The difference maps among zero-filled reconstructions of prospective and retrospective undersampling, and fully sampled reconstructions obtained for *in vivo* brain imaging experiments are shown in units of dB, for acceleration factors of R = 2, 4, and 6. The first and the second rows show the difference maps with respect to fully sampled k-space reconstruction. The last row shows the difference between the zero-filled reconstructions of prospective and retrospective undersampling. As expected, the error increases for both prospective and retrospective undersampling as the acceleration factor increases.